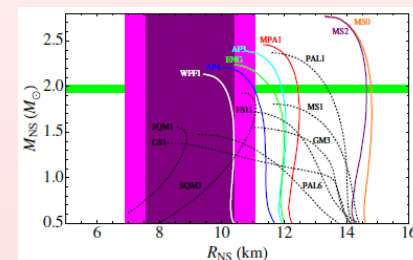


On the Determination of Neutron Star Radii by Observation

Measurement of the Radius of Neutron Stars with High Signal-to-Noise Quiescent Low-Mass X-Ray Binaries in Globular Clusters

Sebastien Guillot *et al.*, *Astrophys. J.* 772, 7(2013)

<http://iopscience.iop.org/0004-637X/772/1/7>

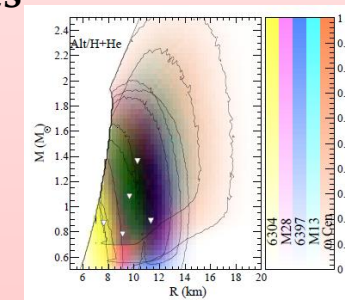
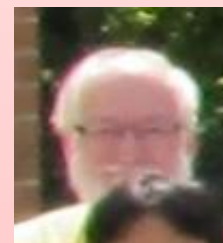


$9.1^{+1.3}_{-1.5}$ km !

Neutron Star Masses and Radii from Quiescent Low-Mass X-Ray Binaries

J.M. Lattimer and A.W. Steiner, *arXiv.1305.3242v1* (2013).

<http://arxiv.org/abs/1305.3242>

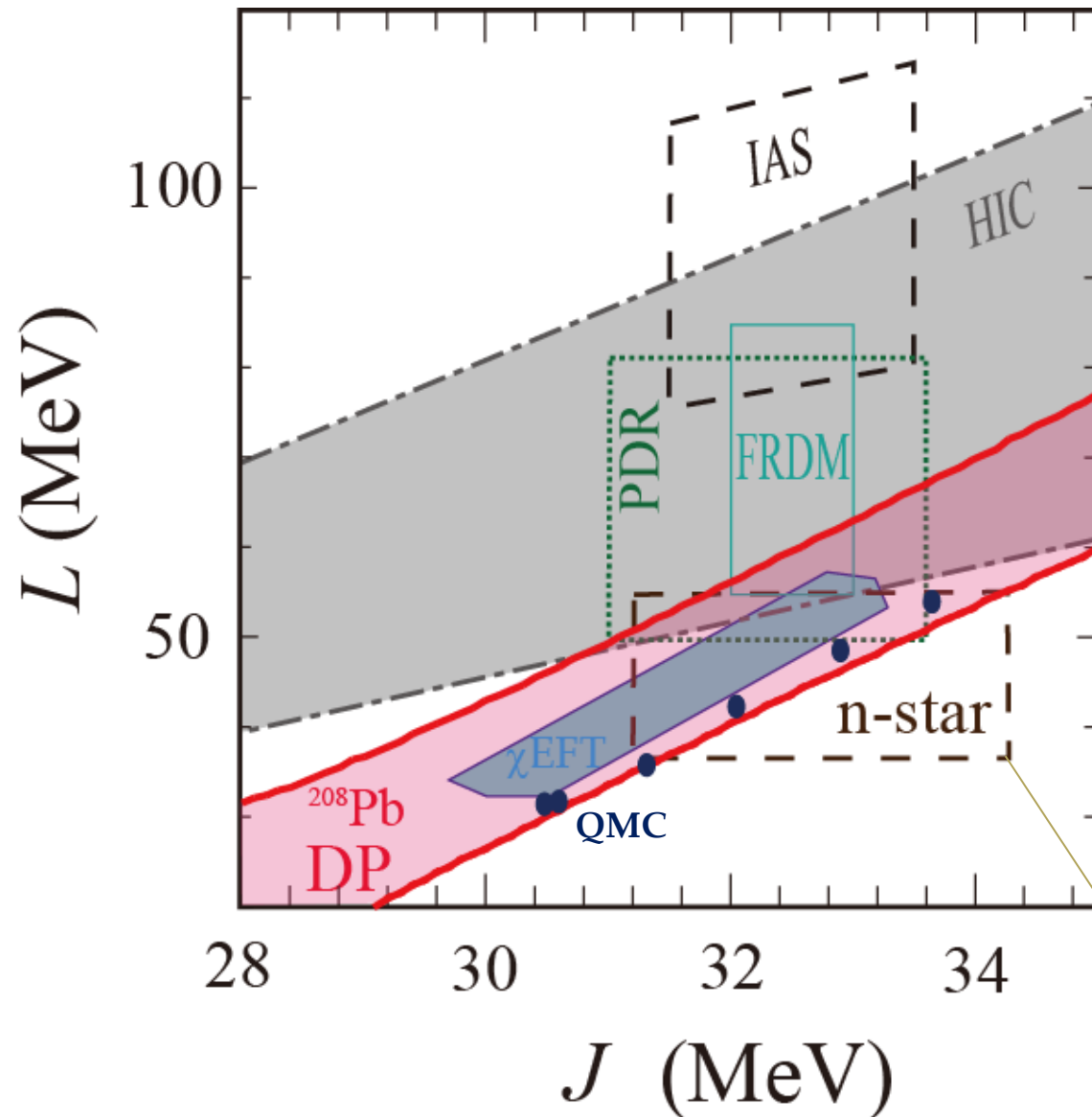


12.1 ± 0.7 km !

3rd International Symposium on Nuclear Symmetry Energy
(NumSym13) NSCL/FRIB, East Lansing, Michigan
July 22 - 26, 2013



Constraints on Symmetry Energy Parameters J and L of Nuclear Equation of State



M.B. Tsang *et al.*,
PRC86, 015803 (2012).

I. Tews *et al.*, PRL110,
032504 (2013)

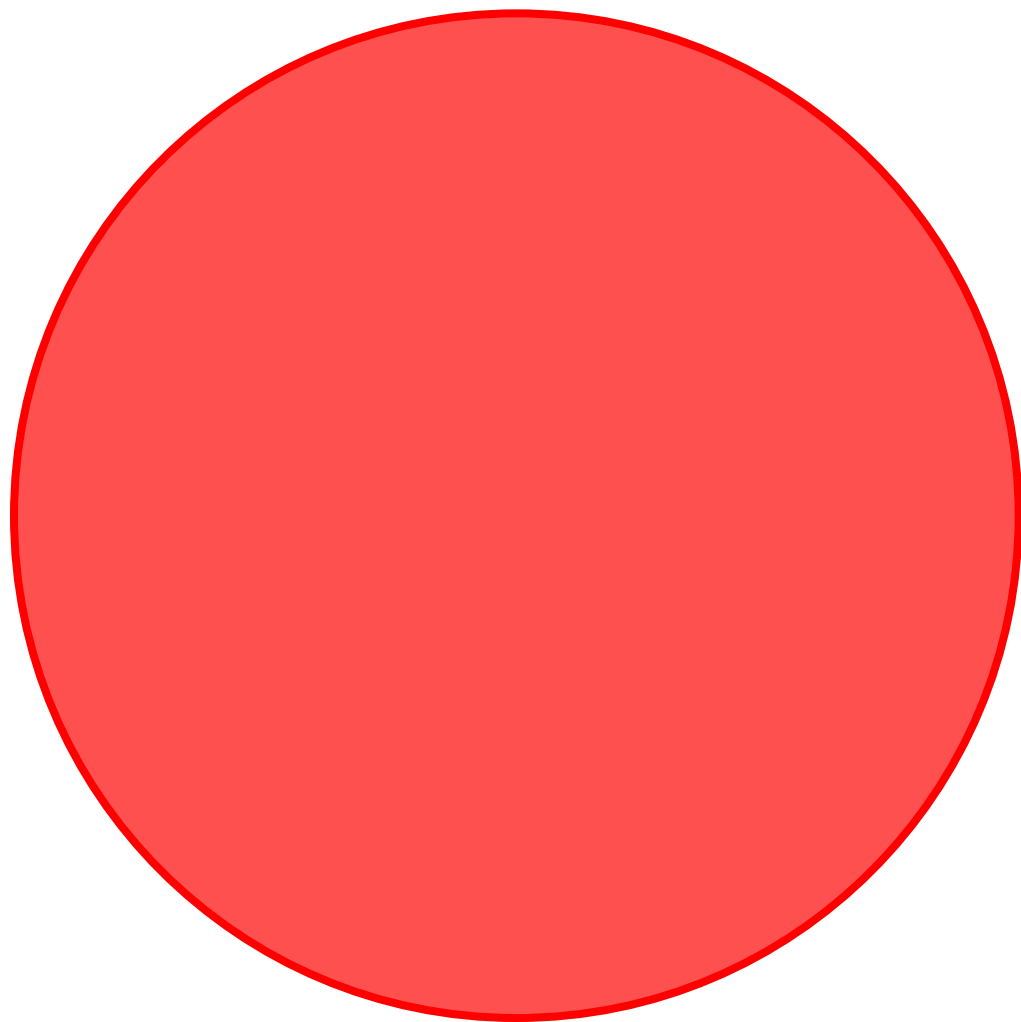
DP: Dipole Polarizability
HIC: Heavy Ion Collision
PDR: Pygmy Dipole Resonance
IAS: Isobaric Analogue State
FRDM: Finite Range Droplet
Model (nuclear mass analysis)
n-star: Neutron Star Observation
 χEFT : Chiral Effective Field Theory
QMC by S. Gandolfi *et al.*,

A.W. Steiner, J. M. Lattimer,
and E.F. Brown

Presentation by AT at NuSym13

The Radius of Neutron Stars

Bob Rutledge, Sebastien Guillot (McGill)
Matthieu Servillat (CNRS), Natalie Webb (Toulouse)



Sun $1 M_{\odot}$

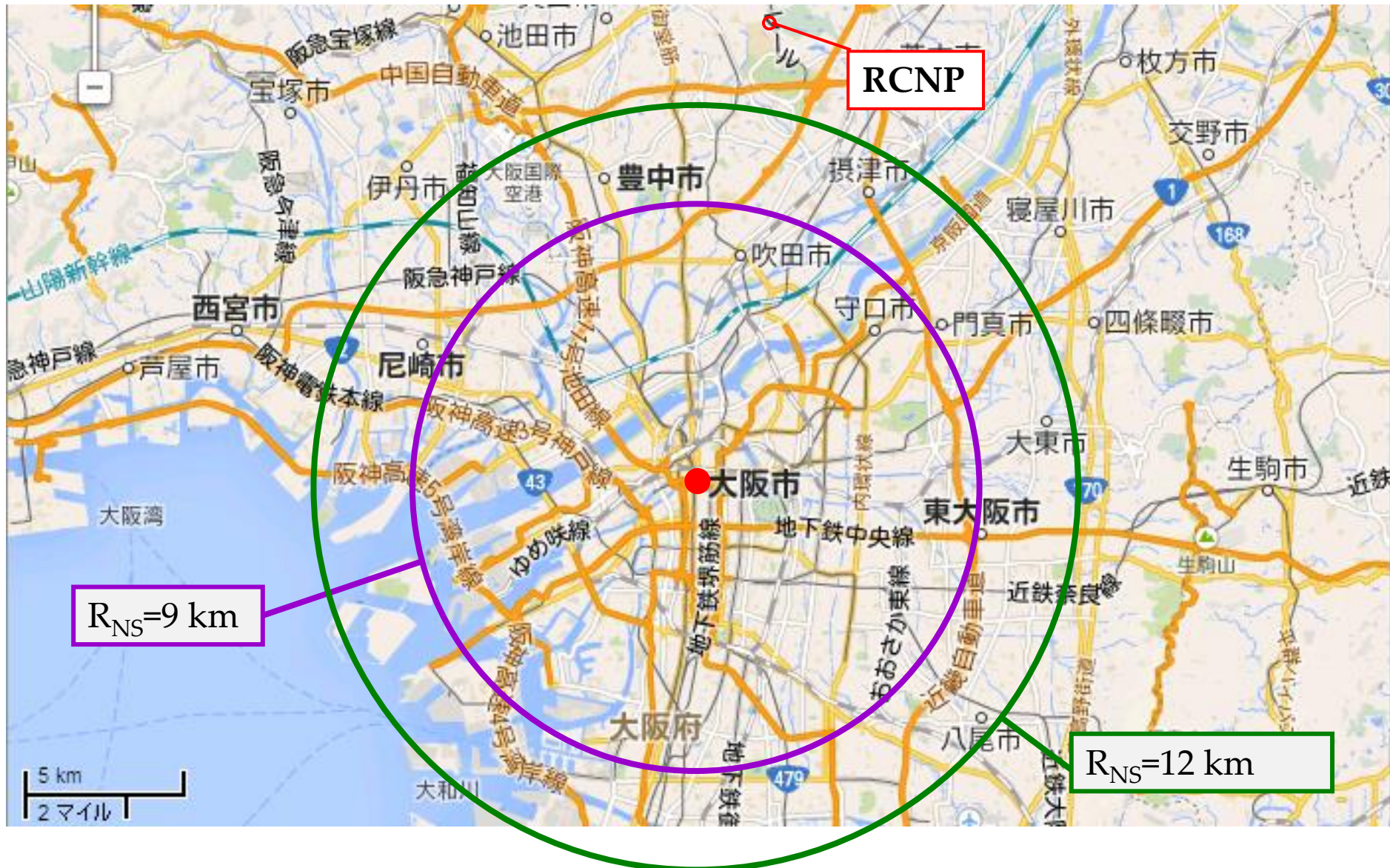


Earth

110 times larger than the earth

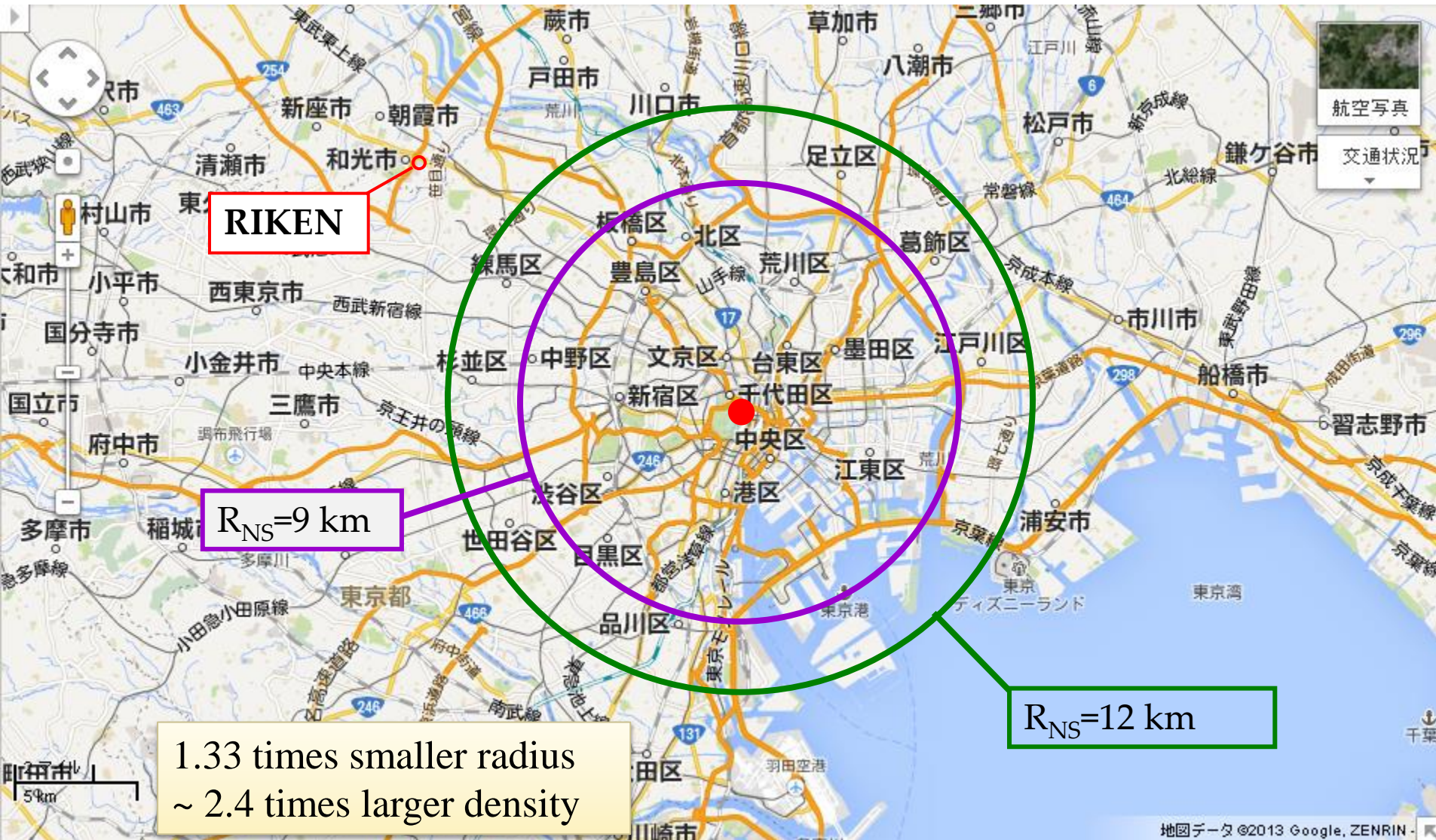
Size of a Neutron Star

$1.4 M_{\odot}$



Size of a Neutron Star

$1.4 M_{\odot}$



MEASUREMENT OF THE RADIUS OF NEUTRON STARS WITH HIGH SIGNAL-TO-NOISE QUIESCENT LOW-MASS X-RAY BINARIES IN GLOBULAR CLUSTERS

SEBASTIEN GUILLOT¹, MATHIEU SERVILLAT^{2,3}, NATALIE A. WEBB^{4,5}, AND ROBERT E. RUTLEDGE¹

¹ Department of Physics, McGill University, 3600 rue University, Montreal, QC, H2X-3R4, Canada; guillots@physics.mcgill.ca, rutledge@physics.mcgill.ca

² Laboratoire AIM (CEA/DSM/IRFU/Sap, CNRS, Université Paris Diderot), CEA Saclay, Bat. 709, F-91191 Gif-sur-Yvette, France

³ Harvard-Smithsonian Center for Astrophysics, 60 Garden Street, Cambridge, MA 02138, USA

⁴ Université de Toulouse; UPS-OMP; IRAP; Toulouse, France

⁵ CNRS; IRAP; 9 Av. colonel Roche, BP 44346, F-31028 Toulouse cedex 4, France

Received 2013 January 31; accepted 2013 May 29; published 2013 June 27

ABSTRACT

This paper presents the measurement of the neutron star (NS) radius using the thermal spectra from quiescent low-mass X-ray binaries (qLMXBs) inside globular clusters (GCs). Recent observations of NSs have presented evidence that cold ultra dense matter—present in the core of NSs—is best described by “normal matter” equations of state (EoSs). Such EoSs predict that the radii of NSs, R_{NS} , are quasi-constant (within measurement errors, of $\sim 10\%$) for astrophysically relevant masses ($M_{\text{NS}} > 0.5 M_{\odot}$). The present work adopts this theoretical prediction as an assumption, and uses it to constrain a single R_{NS} value from five qLMXB targets with available high signal-to-noise X-ray spectroscopic data. Employing a Markov chain Monte-Carlo approach, we produce the marginalized posterior distribution for R_{NS} , constrained to be the same value for all five NSs in the sample. An effort was made to include all quantifiable sources of uncertainty into the uncertainty of the quoted radius measurement. These include the uncertainties in the distances to the GCs, the uncertainties due to the Galactic absorption in the direction of the GCs, and the possibility of a hard power-law spectral component for count excesses at high photon energy, which are observed in some qLMXBs in the Galactic plane. Using conservative assumptions, we found that the radius, common to the five qLMXBs and constant for a wide range of masses, lies in the low range of possible NS radii, $R_{\text{NS}} = 9.1^{+1.3}_{-1.5}$ km (90%-confidence). Such a value is consistent with low- R_{NS} equations of state. We compare this result with previous radius measurements of NSs from various analyses of different types of systems. In addition, we compare the spectral analyses of individual qLMXBs to previous works.

Key words: globular clusters: individual (M28, M13, NGC 5139, NGC 6304, NGC 6397) – stars: neutron – X-rays: binaries

Neutron Star Masses and Radii from Quiescent Low-Mass X-ray Binaries

James M. Lattimer

*Department of Physics and Astronomy, State University of New York at Stony Brook, Stony Brook, NY
11794-3800, USA*

james.lattimer@stonybrook.edu

Andrew W. Steiner

Institute for Nuclear Theory, University of Washington, Seattle, WA 98195, USA

steiner3@uw.edu

ABSTRACT

A recent analysis (Guillot et al. 2013) of the thermal spectra of 5 quiescent low-mass X-ray binaries in globular clusters, in which it was assumed that all neutron stars have the same radius, determined the radius to be $R = 9.1^{+1.3}_{-1.5}$ km to 90% confidence. However, the masses of the sources were found to range from $0.86 M_{\odot}$ to $2.4 M_{\odot}$ and a significant amount of the predicted $M - R$ region violates causality and the existence of a 2 solar mass neutron star. The study determined the amount of Galactic absorption along the lines-of-sight from fitting the X-ray spectra and assumed all sources possessed hydrogen atmospheres. We argue, from a Bayesian analysis, that different interpretations of the data are strongly favored. Our most-favored model assumes i) the equation of state of neutron star crusts is well-understood, ii) the high-density equation of state is consistent with causality and the existence of neutron stars at least as massive as $2 M_{\odot}$, iii) that the Galactic absorption is determined either from the fits in Guillot et al. (2013) or from independent HI surveys, and iv) that these objects are well-described by either hydrogen or helium atmospheres. With these assumptions, the 90% confidence radius range for $1.4 M_{\odot}$ stars is 11.4 to 12.8 km, and the allowed range for radii of all neutron stars between $1.2 M_{\odot}$ and $2.0 M_{\odot}$ is 10.9 to 12.7 km. This result is in much greater agreement with predictions of the equation of state from both nuclear experiments and theoretical neutron matter studies than the smaller radii deduced by Guillot et al. (2013).

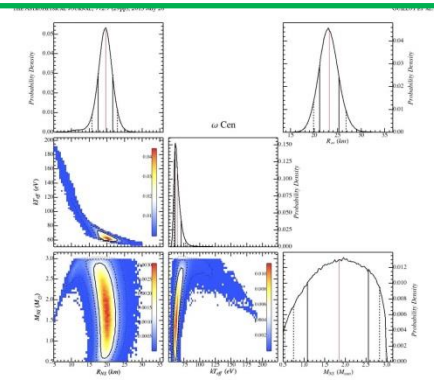


Figure 6. Similar to Figure 3, but for the qLMBX in ω Cen. The physical radius of the NS is $R_{\text{NS}} = 10.6^{+1.1}_{-0.9}$ km which corresponds to $R_{\text{NS}} = 25.2^{+2.6}_{-2.3}$ km, for $N_{\text{H},\text{NS}} = 0.382$.

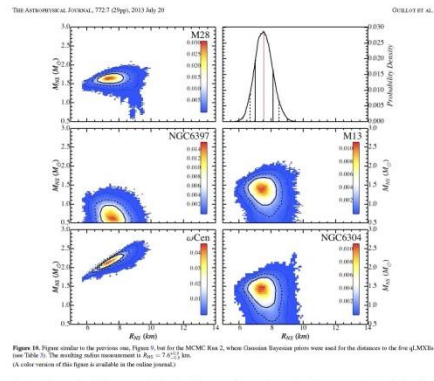
3. For FMS, the dynamical distance has been measured, data = 6.5 ± 0.5 kpc (Rhee 1996). No other paper in the literature has measured this distance, so we have no estimate of the uncertainty. This dynamical measurement is consistent with the value of 6.5 ± 0.5 kpc (Rhee 1996) and the value of 6.5 ± 0.6 kpc (Sundqvist et al. 1996). Sundqvist et al. (1996). While uncertainty could be estimated, we have not done so. We have used the dynamical measurement to permit the limit the effect of dynamical distance on the absolute distance measurement.

4. For Cen's distance was measured in a dynamical study, $d_{\text{Cen}} = 6.5 \pm 0.5$ kpc (Rhee 1996), and no other paper provides a distance with this uncertainty. This measurement is consistent with other measurements of the distance.

5. For NGC 5934, the dynamical distance was measured. However, results from a previous work (Rhee-Bianco et al. 2005), using photometric data from Ptois et al. (2002) are available. In that work, the distance modulus was $M - m = 15.58 \pm 0.07$. The reddening in this work is $E(B - V) = 0.02 \pm 0.01$. The absolute magnitude of the value ($M_{\text{FMS}} = -15.58 \pm 0.07$) (Ptois et al. 2002) can be compared to the accepted value of $M_{\text{FMS}} = -15.58 \pm 0.07$ (Rhee-Bianco et al. 2005). The difference between $E(B - V)$ in the Rhee-Bianco et al. (2005) and the Ptois et al. (2002) is $E(B - V) = 0.02 \pm 0.01$. This difference is a negligible effect on the absolute distance modulus. Therefore, we have used the value of $M - m = 15.58 \pm 0.07$ kpc ($d_{\text{FMS}} = 6.22 \pm 0.26$ kpc).

Overall, the distances to the targeted GCs have uncertainties of $\sim 9\%$ or less, keeping in mind that the distances determined in this work could possibly have systematically underestimated uncertainties.

Individual Fit



that the different value of N_{H1} causes a significantly different resulting R_{95} value. Basically, increasing the assumed value of N_H for a given target leads to a larger R_{95} . This is further discussed in Section 5. In the rest of the present work, the best-fit N_H was fixed at N_{H1} with $M_{\text{bol}} = -19.0$ mag.

Figure 9 shows the marginal and conditional posterior distributions in M_0 - M_1 space for the first four MCMC iterations. The top row shows the marginal distributions for M_0 (left) and M_1 (right). The bottom row shows the conditional distributions for M_0 (left) and M_1 (right). Each plot has R_{0Y} (km) on the x-axis and R_{0X} (km) on the y-axis, both ranging from 0 to 15. Color bars on the right of each plot indicate the probability density, with scales from 0.00 to 0.05 for M_0 and 0.00 to 0.01 for M_1 . Solid lines represent 90% confidence intervals, and dashed lines represent 95% confidence intervals. The distributions are centered around $R_{0Y} \approx 10$ km and $R_{0X} \approx 10$ km.

[illegible]

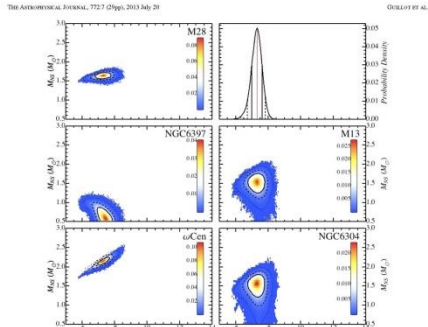


Figure 13. Similar to Figure 9, but for the M28 cluster. The distance is fixed to 10 kpc (black line), and the PL component (with fixed index $\Gamma = 1$) is added to the model, leading to $R_{50} = 1.7 \pm 0.1$ km. (A color version of this figure is available in the online journal.)

and becomes $R_{50} \sim 15\%$ when the temperature is a free parameter. If this is the method used in Gruber et al. (2010), the uncertainties of R_{50} only represent the statistical uncertainties and are therefore highly underestimated. It is inappropriate to keep the temperature fixed because there is no known prior on the NS surface temperature, and therefore it must remain free during the spectral fitting. In addition, the XMM-epi observations suffer from periods of high-background activity which need to be removed from the data. This leads to 34 ks of usable exposure time of the 4 ks available. No such background periods were reported in the original works (Gruber et al. 2010; Webb & Barret 2007). This note about the amount of uncertainty on α Cen is of crucial importance since this source has often been found to be consistent with R_{50} with the best-fit radius measurement available, giving the underestimation $\sim 20\%$ uncertainties on R_{50} . Deeper exposures of α Cen are needed to provide constraints that will be useful for diffraction measurement. Moreover, this discussion also points out the importance of reporting R_{50} and R_{90} (instead of just R_{50}) for the measurements of NS properties using thermal emission from qMXIs.

17

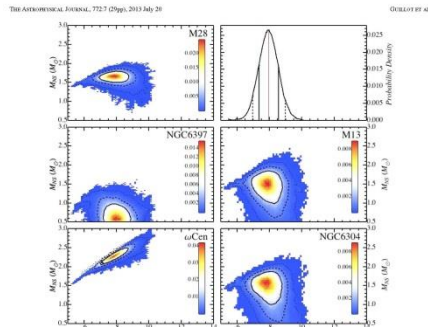


Figure 14. Similar to Figure 9, but for the M28 cluster. The Gaussian Bayesian prior on the distance is included, as well as the PL component (with fixed $\Gamma = 1$) is added to the model, leading to $R_{50} = 1.7 \pm 0.1$ km. (A color version of this figure is available in the online journal.)

observations, and given that more recent calibrations have been used. Similarly to α Cen, deeper exposures of M13 would provide the necessary S/N to constrain the disk.

When the present work was at an advanced stage, results of a spectral analysis of the qMXI in M13 came to our attention (Cassata et al. 2013). These results are consistent with those found in the present work, when normalized to the distance used here.

4.1.4. Comparison with Published Results—M13

The R_{50} value of the qMXI in M13 reported in the discovery paper (Gruber et al. 2010), $R_{50} = 1.2 \pm 0.4$ km (0.7–1.2 keV), corresponds to $R_{50} = 10 \pm 3$ km (0.6–1 keV). This value is consistent with the value presented in the present work, during the spectral fitting. In addition, the XMM-epi observations suffer from periods of high-background activity which need to be removed from the data. This leads to 34 ks of usable exposure time of the 4 ks available. No such background periods were reported in the original works (Gruber et al. 2010; Webb & Barret 2007). This note about the amount of uncertainty on α Cen is of crucial importance since this source has often been found to be consistent with R_{50} with the best-fit radius measurement available, giving the underestimation $\sim 20\%$ uncertainties on R_{50} . Deeper exposures of α Cen are needed to provide constraints that will be useful for diffraction measurement. Moreover, this discussion also points out the importance of reporting R_{50} and R_{90} (instead of just R_{50}) for the measurements of NS properties using thermal emission from qMXIs.

18

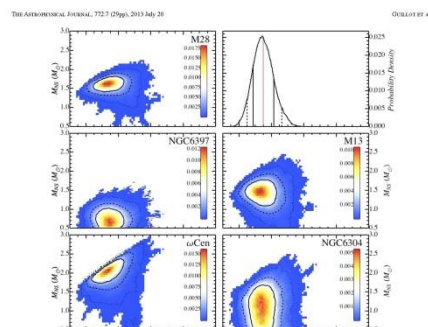


Figure 15. Similar to Figure 9, but for the M28 cluster. The Gaussian Bayesian prior on the distance is included, as well as the PL component (with fixed $\Gamma = 1$) is added to the model, leading to $R_{50} = 1.7 \pm 0.1$ km. (A color version of this figure is available in the online journal.)

4.2.1. Using Gaussian Bayesian Priors for Distances

When adding Gaussian Bayesian priors in place of the fixed distance, the R_{50} contours are as expected, broader in the R_{50} direction. Because the normalization of a thermal spectrum such as α Cen is $(R_{50}/d)^2$, relating the assumptions on d_{50} increases the possible values of R_{50} . This effect is mostly negligible for the two targets observed with the highest S/N, i.e., M28 and NGC 6397. In Run 2, the posterior distribution of R_{50} corresponds to $R_{50} = 7.6 \pm 0.6$ km, broader than that of the previous run.

4.2.2. Adding a Power-law Spectral Component

When adding PL components to account for possible emission of photons at high energy, one finds NS parameters consistent with those of the previous runs. Most PL normalizations are consistent with zero in Runs 4 and 7. For M28, the PL normalization of NGC 6397 in Run 4 and 7, the consistency with zero is only marginal, within 2σ . Finally, in Run 7, the PL normalization of NGC 6397, Norm-sec-4 = $2.7 \times 10^{-5} \text{ keV}^{-1} \text{ cm}^{-2}$, is not consistent with zero. This may indicate the presence of a PL component at large energies and is further discussed in Section 5.

19

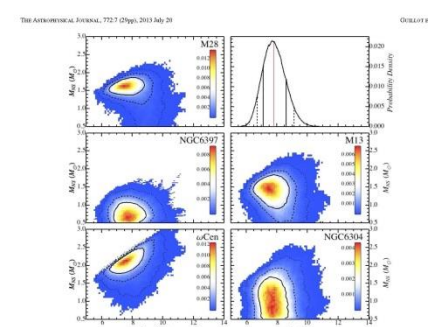


Figure 16. Similar to Figure 9, but for the M28 cluster. The characteristics of this run include R_{50} values free to vary in the fit, and the presence of the Gaussian Bayesian prior for the distance. The PL component was included in Run 4. $R_{50} = 1.7 \pm 0.1$ km. (A color version of this figure is available in the online journal.)

4.2.3. Relating the R_{50} Assumption

As the constraints on the N_{H} parameters are relaxed, the neutron-boss R_{50} parameters remain consistent with those of the previous runs. The posterior distributions of the five R_{50} parameters are consistent with the X-ray deduced R_{50} values found from the spectral fits of the sources individually, i.e., the values used in Run 1–4.

4.2.4. Assumptions Related

For this final run ($R_{50} = 1.7 \pm 0.1$ km) is consistent with the radii obtained in the previous MCMC runs (1–4). The posterior distributions of R_{50} are shown in Figure 15 and detailed in Table 6. Once again, all resulting values are consistent with those of the previous runs. Progressively relating assumptions ensures a good validation of the spectral fit, with an unexpected behavior.

4.2.5. Comparison with nanagrav

We also performed the fit using the model nanagrav instead of *tbabs* for absorption purposes. It has previously been shown that nanagrav and nanagrav produce similar spectral results when fit to experimental data (see Table 4 and Figure 2007). In XSPEC, for the nanagrav model, the R_{50} range is

20

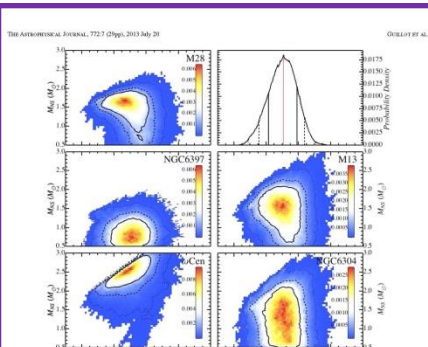


Figure 17. Similar to Figure 9, but for the M28 cluster. All possible assumptions have been added in order to obtain a R_{50} measurement that is least affected by geometry issues. The PL component was included in Run 4. $R_{50} = 1.7 \pm 0.1$ km. (A color version of this figure is available in the online journal.)

17

18

19

20

21

22

23

24

25

26

27

28

29

30

31

32

33

34

35

36

37

38

39

40

41

42

43

44

45

46

47

48

49

50

51

52

53

54

55

56

57

58

59

60

61

62

63

64

65

66

67

68

69

70

71

72

73

74

75

76

77

78

79

80

81

82

83

84

85

86

87

88

89

90

91

92

93

94

95

96

97

98

99

100

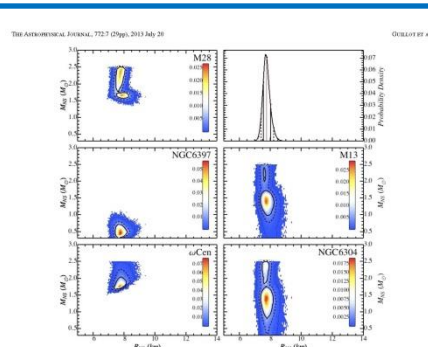


Figure 18. Similar to Figure 9, but for the M28 cluster. All possible assumptions have been added in order to obtain a R_{50} measurement that is least affected by geometry issues. The PL component was included in Run 4. $R_{50} = 1.7 \pm 0.1$ km. (A color version of this figure is available in the online journal.)

17

18

19

20

21

22

23

24

25

26

27

28

29

30

31

32

33

34

35

36

37

38

39

40

41

42

43

44

45

46

47

48

49

50

51

52

53

54

55

56

57

58

59

60

61

62

63

64

65

66

67

68

69

70

71

72

73

74

75

76

77

78

79

80

81

82

83

84

85

86

87

88

89

90

91

92

93

94

95

96

97

98

99

100

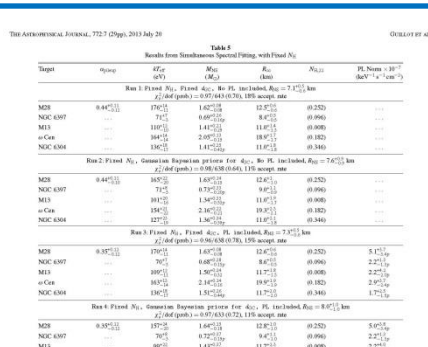


Figure 19. Similar to Figure 9, but for the M28 cluster. All possible assumptions have been added in order to obtain a R_{50} measurement that is least affected by geometry issues. The PL component was included in Run 4. $R_{50} = 1.7 \pm 0.1$ km. (A color version of this figure is available in the online journal.)

17

18

19

20

21

22

23

24

25

26

27

28

29

30

31

32

33

34

35

36

37

38

39

40

41

42

43

44

45

46

47

48

49

50

51

52

53

54

55

56

57

58

59

60

61

62

63

64

65

66

67

68

69

70

71

72

73

74

75

76

77

78

79

80

81

82

83

84

85

86

87

88

89

90

91

92

93

94

95

96

97

98

99

100

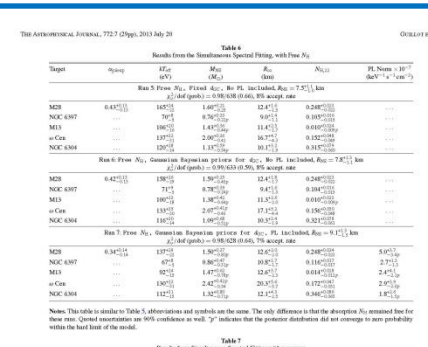


Figure 20. Similar to Figure 9, but for the M28 cluster. All possible assumptions have been added in order to obtain a R_{50} measurement that is least affected by geometry issues. The PL component was included in Run 4. $R_{50} = 1.7 \pm 0.1$ km. (A color version of this figure is available in the online journal.)

17

18

19

20

21

22

23

24

25

26

27

28

29

30

31

32

33

34

35

36

37

38

39

40

41

42

43

44

45

46

47

48

49

50

51

52

53

54

55

56

57

58

59

60

61

62

63

64

65

66

67

68

69

70

71

72

73

74

75

76

77

78

79

80

81

82

83

84

85

86

87

88

89

90

91

92

93

94

95

96

97

98

99

100

THE AMERICAN JOURNAL, Vol. 1 (29th), 2011 July 20

from the
that goos past
et al. 1990;
the $M_{500}-R_{500}$
its of MCMC
 M_{500}/c^2 , i.e.,
those not in
region than
cept causality

to produce a lower value for α in the β region for β fixed, and the β value (corrected) a value of α is cited above. We intend to revisit this

classification and produce the uncontaminated s

In addition to q of MXB R_{ph} measurements, found from the analysis of photospheric radius R_{ph} of X-ray bursts. A review of the method used to find from these sources can be found in the literature (Suleimanov et al. 2011b). The LMXBs EXO 1608–52, and 4U 1820–30 were found to have n of the 2σ ranges $R_{\text{ph}} = [7.5\text{--}11.0]$ km (Ozel et al. [7.5–11.5] km (Güver et al. 2010a) and $R_{\text{NS}} =$ (Güver et al. 2010b), respectively. While these pair with what is found in this paper, controversy is the realization that the analysis presented in the q is not internally consistent because the most probes (from Monte-Carlo sampling) led to imaginary q (Steiner et al. 2010). Relaxing the assumption

spheric radius equals the physical radius R_{NS} at to real-valued solutions of M_{max} and R_{max} , and to large

for the stars. Furthermore, it is argued in a later short burst from EXO 1745-248, UL 1608-52 are not appropriate for such analysis because cooling evolution of these sources does not match of passively cooling NSs (Suleimanov et al. 2015). The $M_{\text{NS}}-R_{\text{NS}}$ constraints from type I X-ray bursts considered with these results in mind.

More recently, distance independent constraints were produced from the analysis of the X-ray bursts from the type I X-ray burster GS 1812-12 (2012). That analysis, performed for the gravities ($\log(g) = 14.0, 14.3, 14.6$) and abundances ($0.01 Z_{\text{Fe}}, 0.1 Z_{\text{Fe}}$ and Z_{Fe}) led to 11.5 km . While distance-independent, the results are influenced by the atmosphere composition

For pure He composition, the upper limit of $B_{\text{He}} < 14$ flux (Zhang et al. 2013).

Finally, the multiwavelength spectral energy of the isolated neutron star RX J185635-3754 produce small values of R_{NS} and M_{NS} with no consistent with these values: $R_{\text{NS}} \sim 6$ km and $M_{\text{NS}} \sim 1.1 M_{\odot}$ (Pons et al. 2002). A recent distant the source $d = 125^{+15}_{-15}$ pc (Walter et al. 2010) values: $R_{\text{NS}} = 11.5 \pm 1.2$ km and $M_{\text{NS}} =$ (Steiner et al. 2012). While this result is consistent with the R_{NS} measurement obtained in this paper and

Recently, it was shown that the dISO can be empirically determined by X-ray Bragg measurements of the thermal expansion of quartz (Klein *et al.* 2013). The measured radius of the dISO (R_{dISO}) by X-ray bragg (Steiner *et al.* 2010). This method uses MCMC simulation and Bayesian priors to determine the most probable dISO parameters, and equivalently, the corresponding most probable R_{dISO} for NS. In a recent paper, this method was used with four R_{dISO} for burning sources and four GC of M3Xs. Considering different R_{dISO} values (from 2.5 to 10.5 km) and different GCs (1.5 and 13.92 km (Steiner *et al.* 2013)). The R_{dISO} distribution of the present paper $R_{\text{dISO}} = 9.1^{+1.3}_{-1.1}$ km (90% confidence, from Run 7) is consistent with several of the model variations of Steiner *et al.* (2013), namely variation C (dISO parameterized with uniform prior in the pressure at four energy density values), variation C1 (same as previous, but with low value of the color correction

1. *Journal of the American Medical Association*, 2000; 283: 2689-2696.

Heinke et al. 2006), supplanting stiff diOs, such as MSO₂ (Miller & Serot 1999). Nonetheless, the range of radii allowed by the published $M_{\text{X}}-R_{\text{XO}}$ contours for K7 is consistent with the radius measurement presented in the present work. Moreover the $K7 M_{\text{X}}-R_{\text{XO}}$ contours are compatible with the diOs WFFP (Wings et al. 1988). Another work used the long photometric radius expansion X-ray bursts from AT 1724–307 to conclude that stiff diOs are describing the dense matter inside NSs.

By doing so, the distance uncertainties associated with the series R_{XO} distribution. In addition, one can see series distributions over any parameter $M_{\text{XO}}, R_{\text{XO}}$ distributions, while the grid-constrained can be problematic in the case of sparse parameters and complicated γ -space. This work is an affine-invariant, ensemble called “Stretch-Mo” algorithm, which

The authors would like to thank the referee for that improved the clarity of this article. S.G. is a Graduate Scholar and acknowledges the support of the Vanier CGS program. R.E.R. is supported by Discovery grant. M.S. acknowledges support of Chandra grant G00-13063X and the Centre National de la Recherche Scientifique (CNRS) and the High Energy Astrophysics Archive Research Center (HEAARC). The authors are also indebted to Brad Breton for sharing his python code of the "Stretch-Move" algorithm. Finally, the authors acknowledge the use of archived *XMM* and *Chandra* data from the High Energy Astrophysics Archive Research Center (HEAARC).

Ho, W. C. G., & Heide, C. O. 2009, *Nature*, 462, 71
Hosokawa, C. I., & Nakamura, I. 2001, *PhRvC*, 64, 067802

- ## 6. SUMMARY

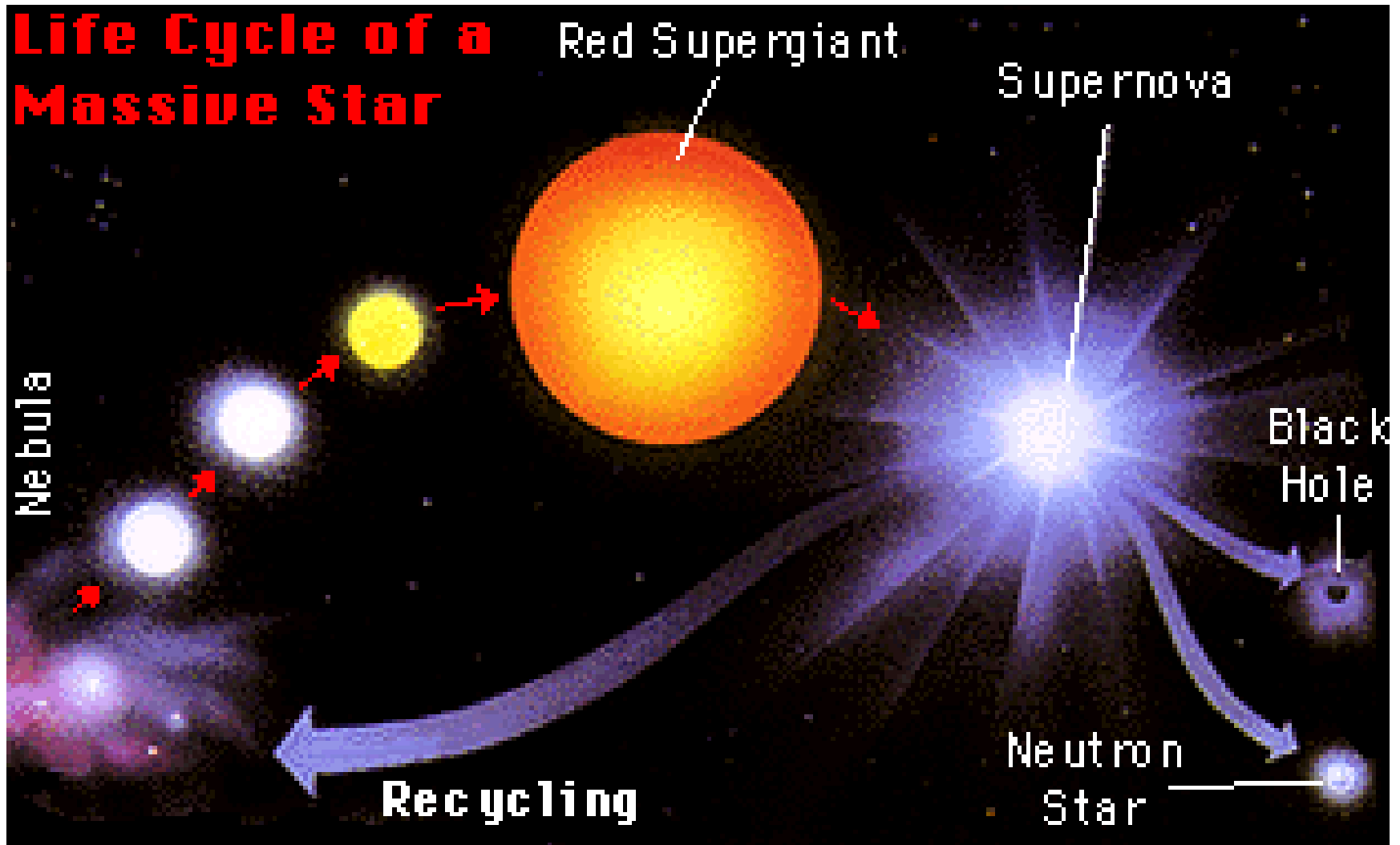
Summary

Geweke, J., & Porter, J. W.: 2016, *Climatic*, 3, 65
Ginsburg, D. E., Evans, I. N., Garfield, K., et al.: 2007, CInSW, 14, 33
Ginsburg, R. G., Camacho, E., Bingham, A., Lucarelli, S., & D'Onofrio, V.: 2019, *A&A*, 571, A88
Gurbel, S. K., & Ribbins, W. J.: 1995, *AAAS*, 150, 293
Gregory, P.: 2005, *Bayesian Logical Data Analysis for the Physical Sciences* (New York: Cambridge Univ. Press)
Hahn, J. and Ost, H. ed.: L. M. Morrison & A. Sampson (San Francisco, CA: ASP), 28
Hornum, R. W.: 1987, *A&J*, 113, 718
Kleinman, L., Petri, G., Sarazin, F., & Apicciato, A.: 2020, *A&AS*, 344, 5
Rutledge, R. E., Ribbins, L., Brown, E. F., Paxton, G. G., & Zarlin, V. E.: 1999, *A&J*, 514, 945
Rutledge, R. E., Ribbins, L., Brown, E. F., Paxton, G. G., & Zarlin, V. E.

Introduction

Pages 1-3

Stellar Evolution of a Massive Star



Core-Collapse Supernova and Formation of a Neutron Star

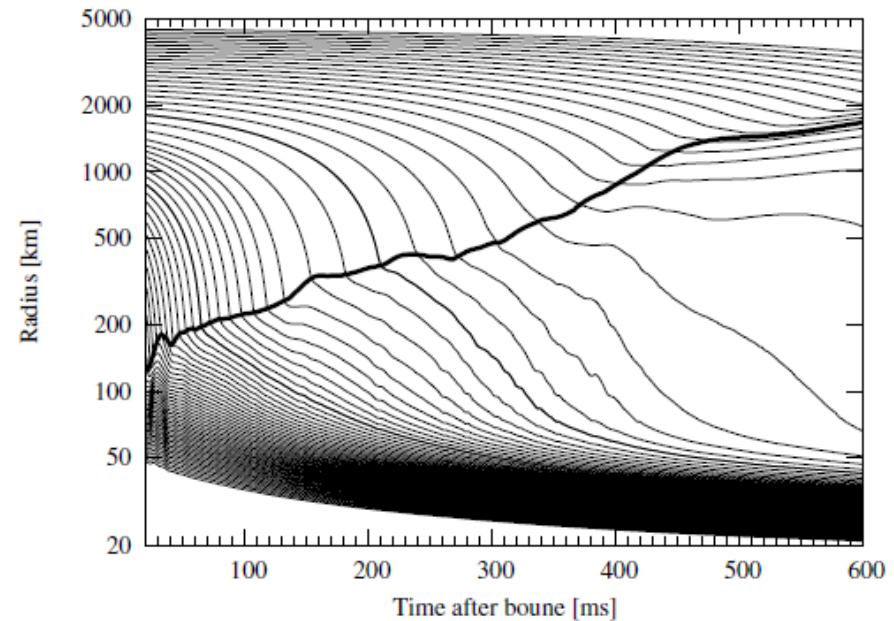
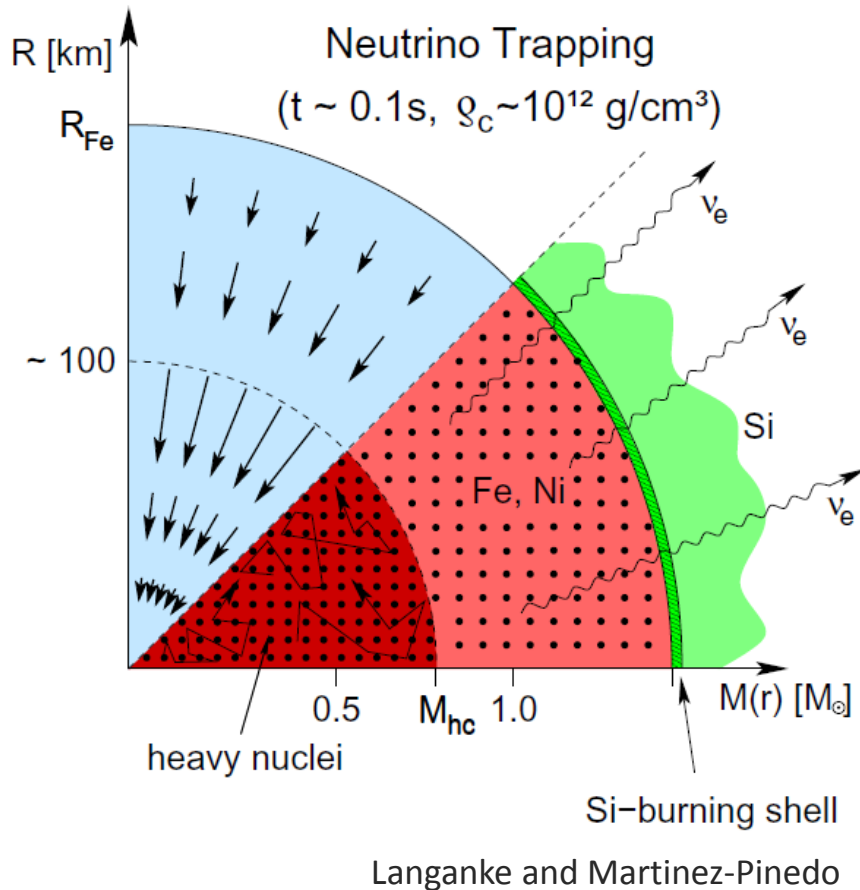


Figure 6. Mass trajectory as a function of time after the bounce for 2D simulation of $15 M_\odot$ with LS180. The thick black line represents the angle-averaged shock radius. The gray lines show the mass from 1.0 to $1.7 M_\odot$ at intervals of $0.01 M_\odot$. Two thin black lines indicate 1.4 and $1.5 M_\odot$, respectively.

Y. Suwa et al., ApJ764, 99 (2013).

A star collapses due to gravitational force forming a neutron star if the mass of the star exceeds the Chandrasekhar limit of $\sim 1.44 M_\odot$.

One of modern 2D simulations, successful of making supernova explosion

Neutron Star

the densest material in the universe

Fundamental Questions:

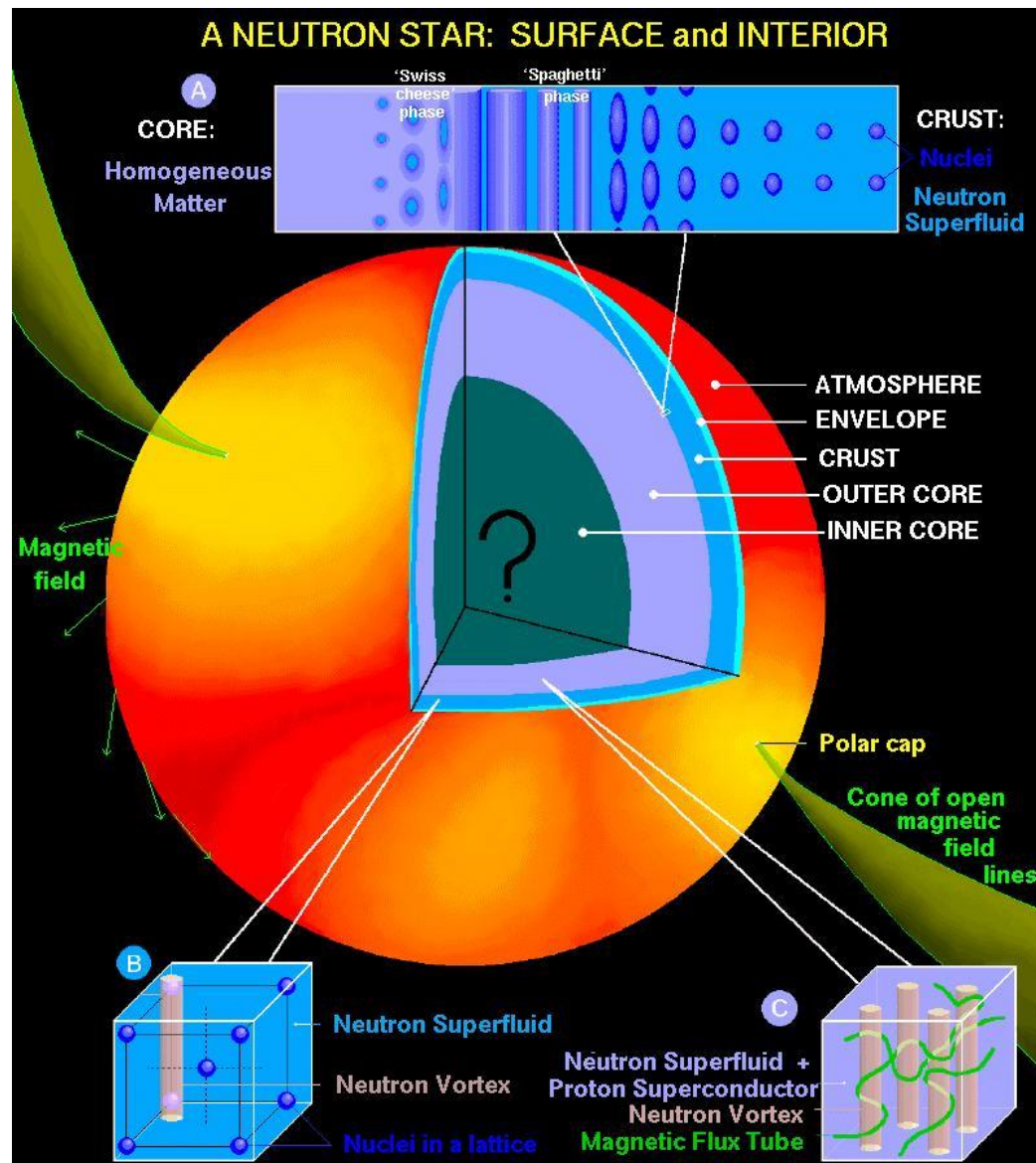
How large and how stiff is a neutron star?

What is the internal structure of a neutron star?

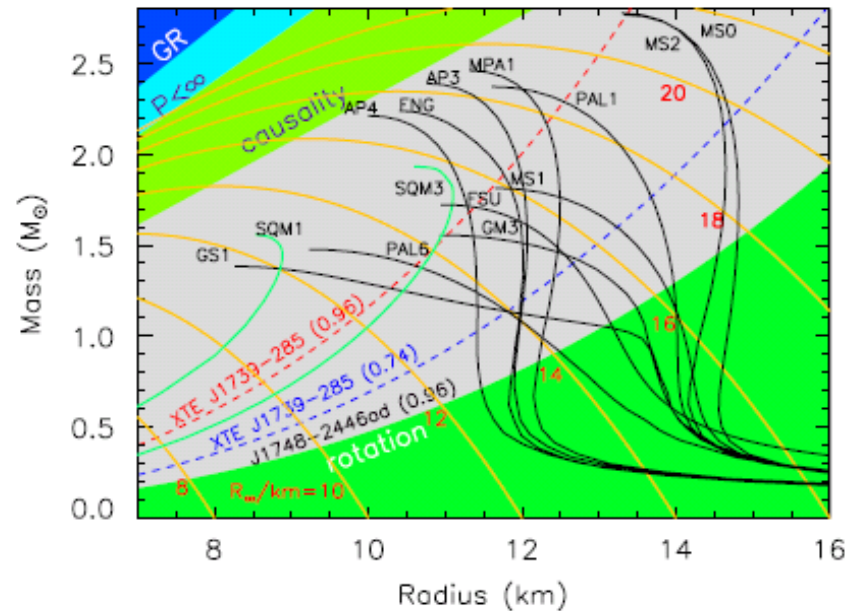
How much fraction of protons and electrons exist?

Meson condensation? Hyperons? deconfined quark matter? in the core.

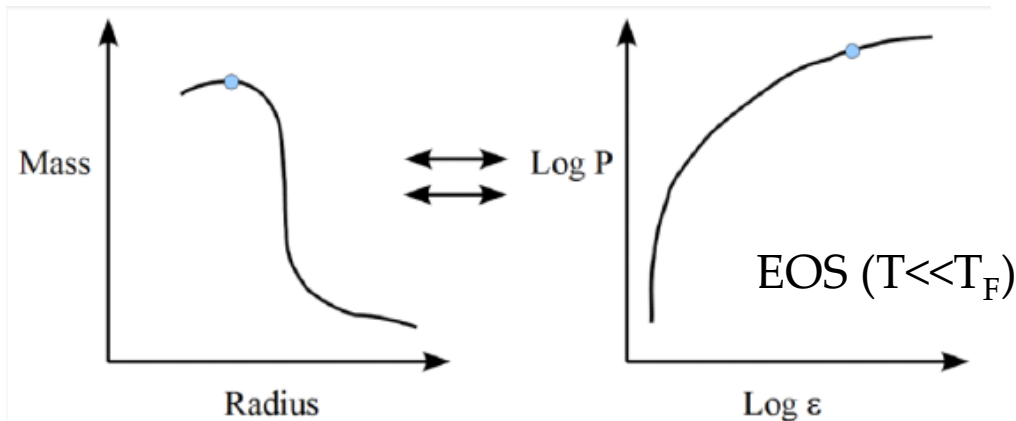
In order to answer to these questions, we need know the equation of state of the dense nuclear matter, especially for neutron rich matter.



Neutron Star Mass-Radius Relation and Nuclear Equation of State



Lattimer et al., Phys. Rep. 442, 109(2007)



- Unlike planets, neutron stars form a one-dimensional family
- Neutron stars (to better than 10%) all lie on one universal mass-radius curve

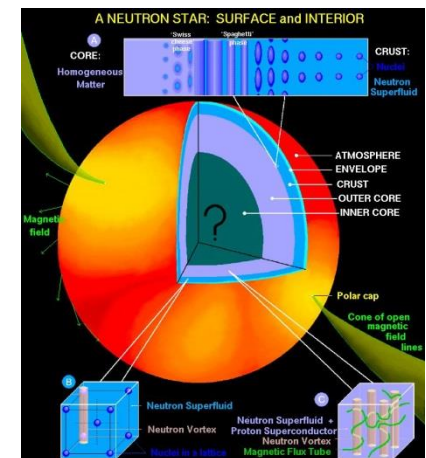
Tolman-Oppenheimer-Volkoff (TOV) equation

The TOV equation constrains the structure of a spherically symmetric body in static gravitational equilibrium in general relativity.

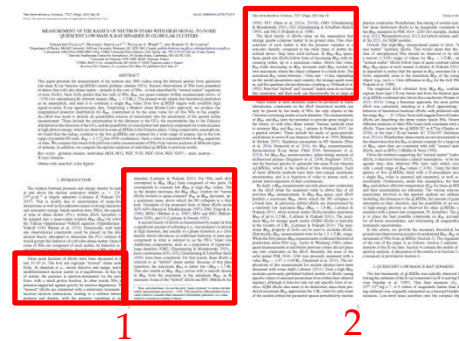
It predicts an upper bound to the mass of stars composed of neutron-degenerate matter (*i.e.* neutron stars)

The mass is considered to be around 1.5-3.0 solar mass.

$$\frac{dP(r)}{dr} = -\frac{G}{r^2} \left[\rho(r) + \frac{P(r)}{c^2} \right] \left[M(r) + 4\pi r^3 \frac{P(r)}{c^2} \right] \left[1 - \frac{2GM(r)}{c^2 r} \right]^{-1}$$



Families of Nuclear EOS



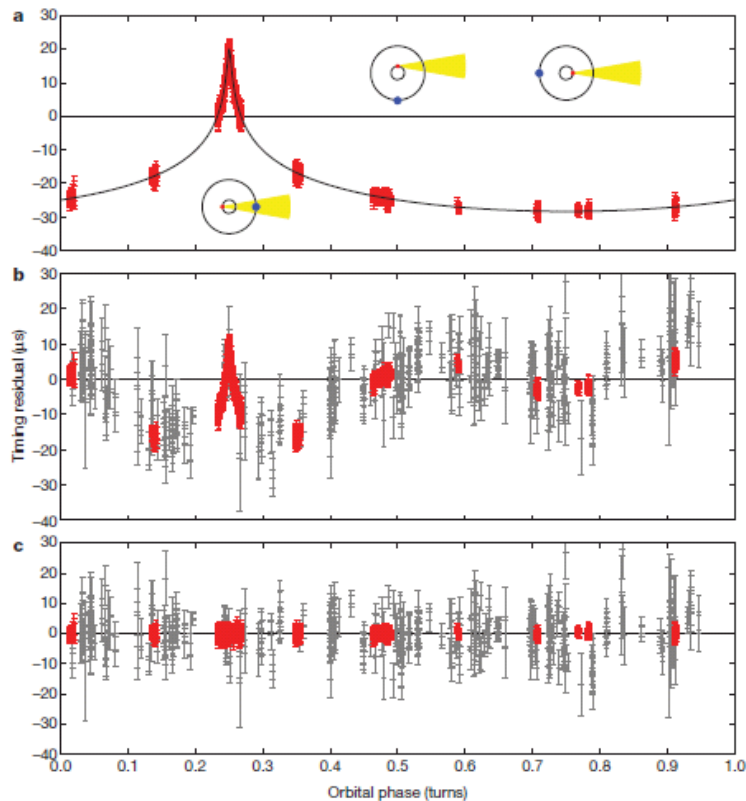
1. “normal” dense matter
neutrons, and a fraction of protons and electrons
2. “hybrid” dense matter, softening at high-densities,
additional hadronic or pure-quark component in “inner core”
(e.g. hyperons)
3. strange quark matter
pressure vanishes at non-zero density \rightarrow solid surface
increasing mass with increasing radius

Observation of a Two Solar-Mass Neutron Star Excluded Present EOS Models with Strangeness

P.B. Demorest et al., Nature 467, 1081(2010)

J1614-2230

$(1.97 \pm 0.04)M_{\odot}$ inclination: $89.17 \pm 0.02^{\circ}$



Observation of **Shapiro-delay** of pulsar signals of a neutron star - white dwarf binary.

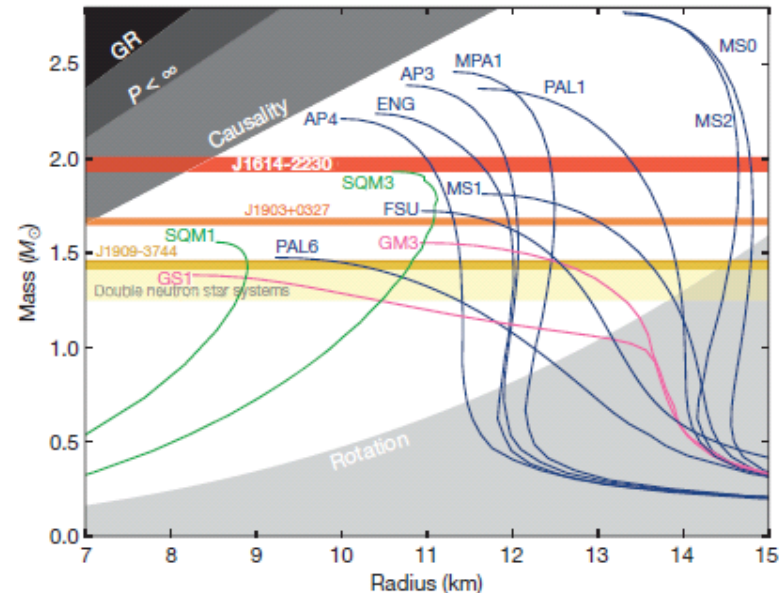


Figure 3 | Neutron star mass-radius diagram. The plot shows non-rotating mass versus physical radius for several typical EOSs²⁷: blue, nucleons; pink, nucleons plus exotic matter; green, strange quark matter. The horizontal bands show the observational constraint from our J1614-2230 mass measurement of $(1.97 \pm 0.04)M_{\odot}$, similar measurements for two other millisecond pulsars^{8,28} and the range of observed masses for double neutron star binaries². Any EOS line that does not intersect the J1614-2230 band is ruled out by this measurement. In particular, most EOS curves involving exotic matter, such as kaon condensates or hyperons, tend to predict maximum masses well below $2.0M_{\odot}$ and are therefore ruled out. Including the effect of neutron star rotation increases the maximum possible mass for each EOS. For a 3.15-ms spin period, this is a $\lesssim 2\%$ correction²⁹ and does not significantly alter our conclusions. The grey regions show parameter space that is ruled out by other theoretical or observational constraints². GR, general relativity; P , spin period.

Blue: nucleons

Pink: nucleons and exotic matter

Green: strange quark matter

Another Observation of a Two Solar-Mass Neutron Star

Not Referenced

J0348+0432

$2.01 \pm 0.04 M_{\odot}$

J. Antoniadis et al., Science 340, 448 (2013)

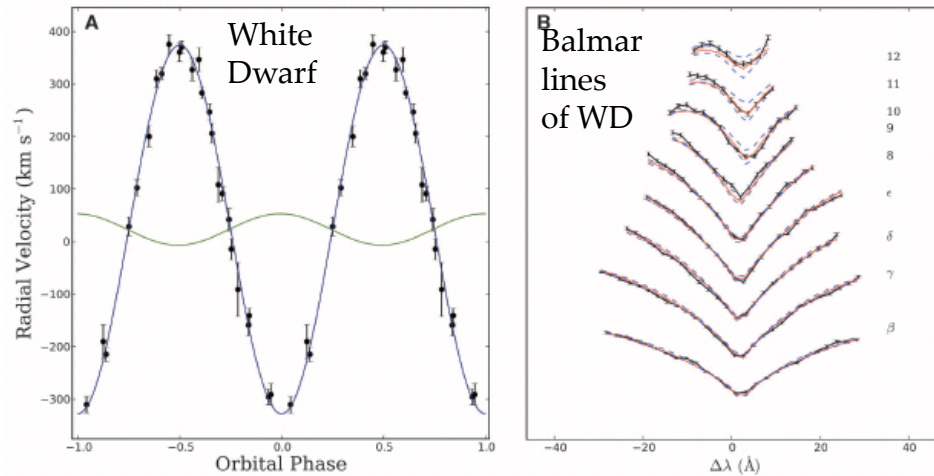


Fig. 1. Radial velocities and spectrum of the white dwarf companion to PSR J0348+0432. (A) Radial velocities of the WD companion to PSR J0348+0432 plotted against the orbital phase (shown twice for clarity). Overplotted is the best-fit orbit of the WD (blue line) and the mirror orbit of the pulsar (green). Error bars indicate 1- σ confidence intervals. (B) Details of the fit to the Balmer lines (H β to H12) in the average spectrum of the WD companion to PSR J0348+0432 created by the coherent addition of 26 individual spectra shifted to zero velocity. Lines from H β (bottom) to H12 are shown. The red solid lines are the best-fit atmospheric model (see text). Two models, one with $T_{\text{eff}} = 9900$ K and $\log g = 5.70$ and one with $T_{\text{eff}} = 10,200$ K and $\log g = 6.30$, each $\sim 3\text{-}\sigma$ off from the best-fit central value (including systematics), are shown for comparison (dashed blue lines).

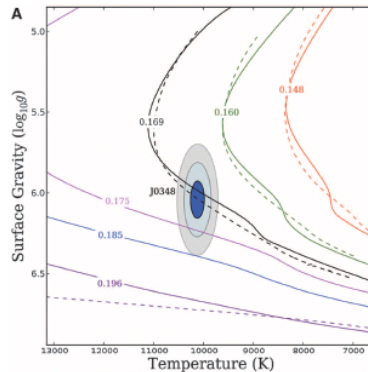


Fig. 2. Mass measurement of the white dwarf companion to PSR J0348+0432. (A) Constraints on T_{eff} and g for the WD companion to PSR J0348+0432 compared with theoretical WD models. The shaded areas depict the $\chi^2 - \chi^2_{\text{min}} = 2.3$, 6.2, and 11.8 intervals (equivalent to 1-, 2-, and 3- σ) of our fit to the average spectrum. Dashed lines show the detailed theoretical

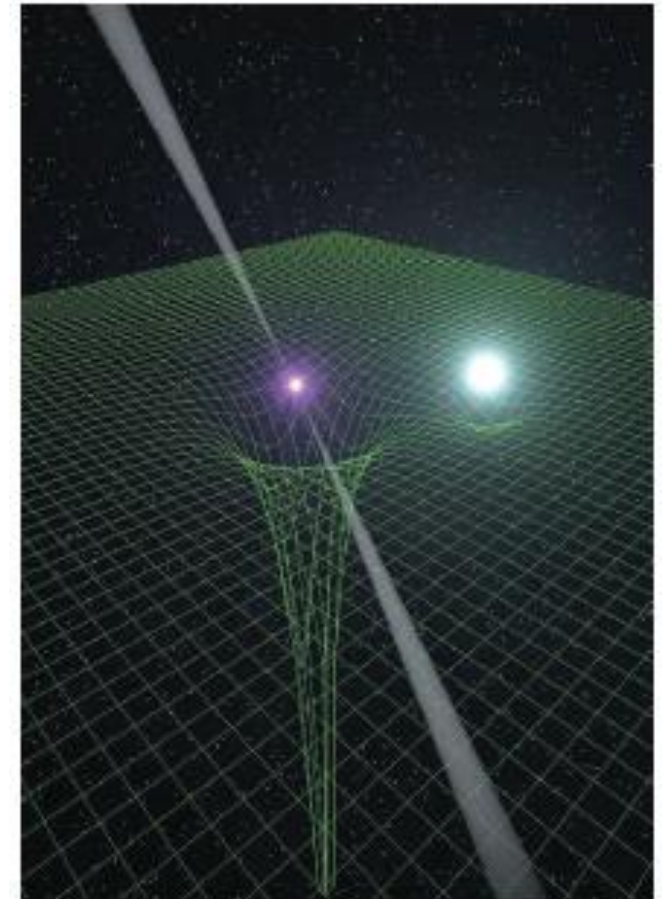
$$K_{\text{WD}} = 351 \pm 4 \text{ km s}^{-1}$$

$$K_{\text{PSR}} = 30.008235 \pm 0.000016 \text{ km s}^{-1}$$

$$M_{\text{PSR}} / M_{\text{WD}} = K_{\text{WD}} / K_{\text{PSR}} = 11.70 \pm 0.13$$

$$T_{\text{eff}} = 10120 \pm 47_{\text{stat}} \pm 90_{\text{sys}} \text{ K}$$

$$\log_{10}(g [\text{cm s}^{-2}]) = 6.035 \pm 0.032_{\text{stat}} \pm 0.060_{\text{sys}}$$



Artist's impression of the PSR J0348+0432 system. The compact pulsar (with beams of radio emission) produces a strong distortion of spacetime (illustrated by the green mesh). Conversely, spacetime around its white dwarf companion (in light blue) is substantially less curved. According to relativistic theories of gravity, the binary system is subject to energy loss by gravitational waves.

The Work of G13

The primary motivation is to measure the **NS radius** from observation data, and to extract constraints on the **dense equation of state** (dEOS).

G13 assumes that **the NS radius is constant**, as a quasi-constant mass is predicted within a large range of NS masses in “normal” EOSs.

A radius is obtained to give the smallest chi-square for reproducing the **spectra of five qLMXBs**.

Excluding data with unqualified errors for extracting a reliable systematic uncertainty of the NS radius.

Methods to Measure M_{NS} and R_{NS}



2

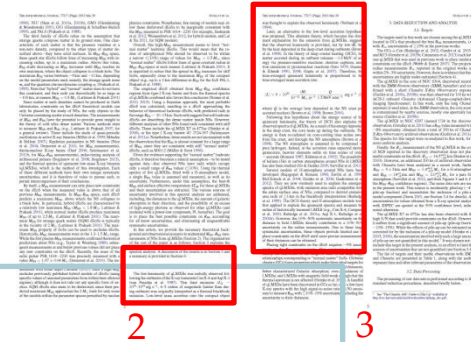
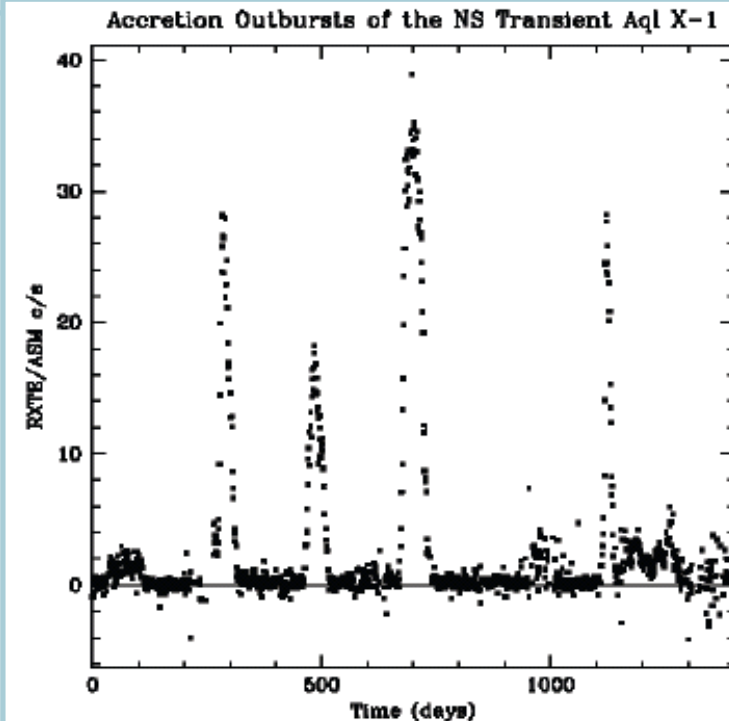
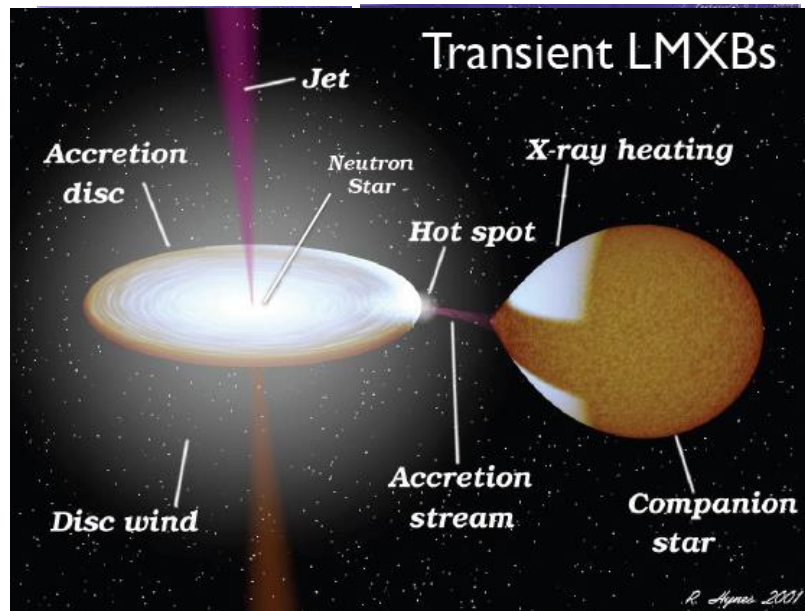
- quasi-periodic oscillations in active X-ray binaries
- Keplerian parameters in NS binaries
- thermonuclear X-ray bursts
- pulse timing analysis of millisecond pulsars
- thermal spectral of quiescent low-mass X-ray binaries

Quiescent Low-Mass X-Ray Binary (qLMXB)

Low Mass X-Ray Binary (LMXB) 低質量X線連星 is a binary star where one of the components is either a black hole or a neutron star.

The word *Quiescent* means *inactive* or more-specifically *low-luminosity* phase. X-Ray emission from a qLMXB star is 4-5 orders of magnitude fainter than during outburst.

Cen X-4 and Aql X-1: van Paradijs et al . (1987)



Globular Clusters 球状星团

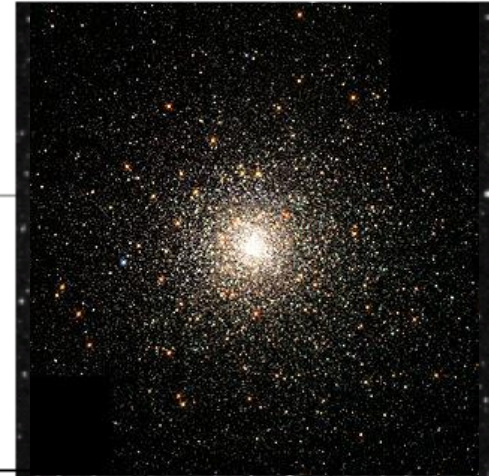
Globular clusters are spherical collection of stars, which are tightly bound by the gravitational force, that orbits a galactic core. 10^5 - 10^6 stars

All the stars in a globular cluster are at nearly the same distance from the earth.

Distance of globular clusters are relatively accurately measured by observing standard candles, e.g. RR-Lyrae or Cepheids, or by parallax measurement.



3



NGC	D (kpc)	+/- (%)
104	5.13	4
288	9.77	3
362	10.0	3
4590	11.22	3
5904	8.28	3
7099	9.46	2
6025	7.73	2
6341	8.79	3
6752	4.61	2

Carretta et al (2000)

How R_{NS} is Measured: the Essence

$$F \sim \sigma T^4 \frac{R^2}{D^2} \quad \text{for the case of black-body radiation}$$

F : flux of radiation, more-simply brightness

R : (radiation) radius [†]

D : distance

T : temperature

σ : Stefan-Boltzmann coefficient ($5.67 \times 10^{-8} \text{ W m}^{-2} \text{ K}^{-4}$)

In a realistic calculation one needs:

- radiation spectral model (difference from black-body)
- radiation attenuation (Galactic absorption)
- radiation radius to radius conversion (general relativity)
- red-shift correction
- mass-radius relation (EOS)

[†]The entire surface of a NS is assumed as the emission area.

Radiation Radius

in general relativity

radiation (apparent) radius, or angular emission area

$$R_{\infty} = R_{\text{NS}} \left(1 - \frac{r_g}{R_{\text{NS}}} \right)^{-1/2}$$

Schwarzschild radius

$$r_g \equiv \frac{2GM_{\text{NS}}}{c^2} \approx 2.95 \frac{M_{\text{NS}}}{M_{\text{sun}}} \text{ km}$$

Deep Crustal Heating (DCH)

E.F. Brown et al., ApJ 504, L95(1998)

Radiation energy during the quiescent time:

from energy deposit of accreting mass
during outburst. 1.47 MeV/nucleon

Pressure dependent reactions in deep crust

electron captures
neutron emission
pynonuclear fusion

Heat conduction from the core:

of the order of 10^4 year

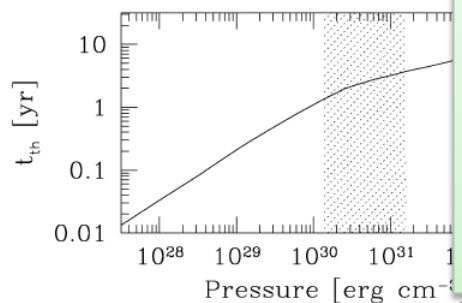
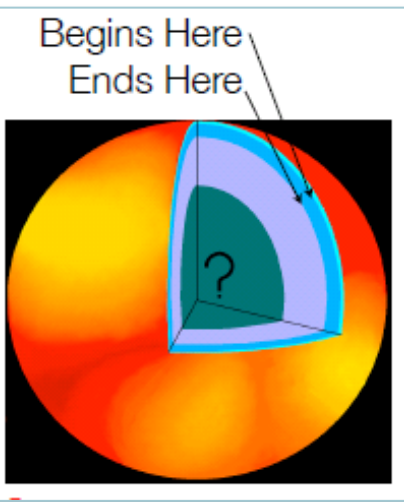


FIG. 1.—Timescale for heat to diffuse from a given pressure to the surface (eq. [3]) for a neutron star ($R = 10$ km, $M = 1.4 M_{\odot}$) accreting at $\dot{M} = 10^{-11} M_{\odot} \text{ yr}^{-1}$. Most of the nuclear energy (98%) is released in the shaded region. The change in slope at the shaded region is caused by a reduction in the electron to baryon ratio. At $P > 10^{31} \text{ erg cm}^{-3}$, the pressure goes from electron dominated to neutron dominated.

Table 1. Non-equilibrium processes in the outer crust

P (dyn cm $^{-2}$)	ρ (g cm $^{-3}$)	Reaction	$\Delta\rho/\rho$	total heat (MeV/nucleon)	deposited heat (MeV/nucleon)
$7.235 \cdot 10^{26}$	$1.494 \cdot 10^9$	$^{56}\text{Fe} \rightarrow ^{56}\text{Cr} - 2e^- + 2\nu_e$	0.08	0.04	0.01
$9.569 \cdot 10^{27}$	$1.114 \cdot 10^{10}$	$^{56}\text{Cr} \rightarrow ^{56}\text{Ti} - 2e^- + 2\nu_e$	0.09	0.04	0.01
$1.152 \cdot 10^{29}$	$7.848 \cdot 10^{10}$	$^{56}\text{Ti} \rightarrow ^{56}\text{Ca} - 2e^- + 2\nu_e$	0.10	0.05	0.01
$4.747 \cdot 10^{29}$	$2.496 \cdot 10^{11}$	$^{56}\text{Ca} \rightarrow ^{56}\text{Ar} - 2e^- + 2\nu_e$	0.11	0.05	0.01
$1.361 \cdot 10^{30}$	$6.110 \cdot 10^{11}$	$^{56}\text{Ar} \rightarrow ^{52}\text{S} + 4n - 2e^- + 2\nu_e$	0.12	0.06	0.05

Table 2. Non-equilibrium processes in the inner crust

P (dyn cm $^{-2}$)	ρ (g cm $^{-3}$)	reactions	X_n	$\Delta\rho/\rho$	deposited heat (MeV/nucleon)
$1.980 \cdot 10^{30}$	$9.075 \cdot 10^{11}$	$^{52}\text{S} \rightarrow ^{46}\text{Si} + 6n - 2e^- + 2\nu_e$	0.07	0.13	0.09
$2.253 \cdot 10^{30}$	$1.131 \cdot 10^{12}$	$^{46}\text{Si} \rightarrow ^{40}\text{Mg} + 6n - 2e^- + 2\nu_e$	0.18	0.14	0.10

The time-averaged quiescent
luminosity is proportional to the
time-averaged mass fraction rate.
The entire surface of a NS is
considered to be the radiation
emission area.

$1.228 \cdot 10^{31}$	$8.980 \cdot 10^{12}$	$^{54}\text{Si} \rightarrow ^{48}\text{Mg} + 6n - 2e^- + 2\nu_e$	0.76	0.04	0.03
$1.602 \cdot 10^{31}$	$1.127 \cdot 10^{13}$	$^{48}\text{Mg} + ^{48}\text{Mg} \rightarrow ^{96}\text{Cr}$	0.79	0.04	0.11
$1.613 \cdot 10^{31}$	$1.137 \cdot 10^{13}$	$^{96}\text{Cr} \rightarrow ^{88}\text{Ti} + 8n - 2e^- + 2\nu_e$	0.80	0.02	0.01

Data Reduction

Pages 3-12

X-Ray Exposure (Observation) Data

Table 1
X-ray Exposures of the Targeted Clusters

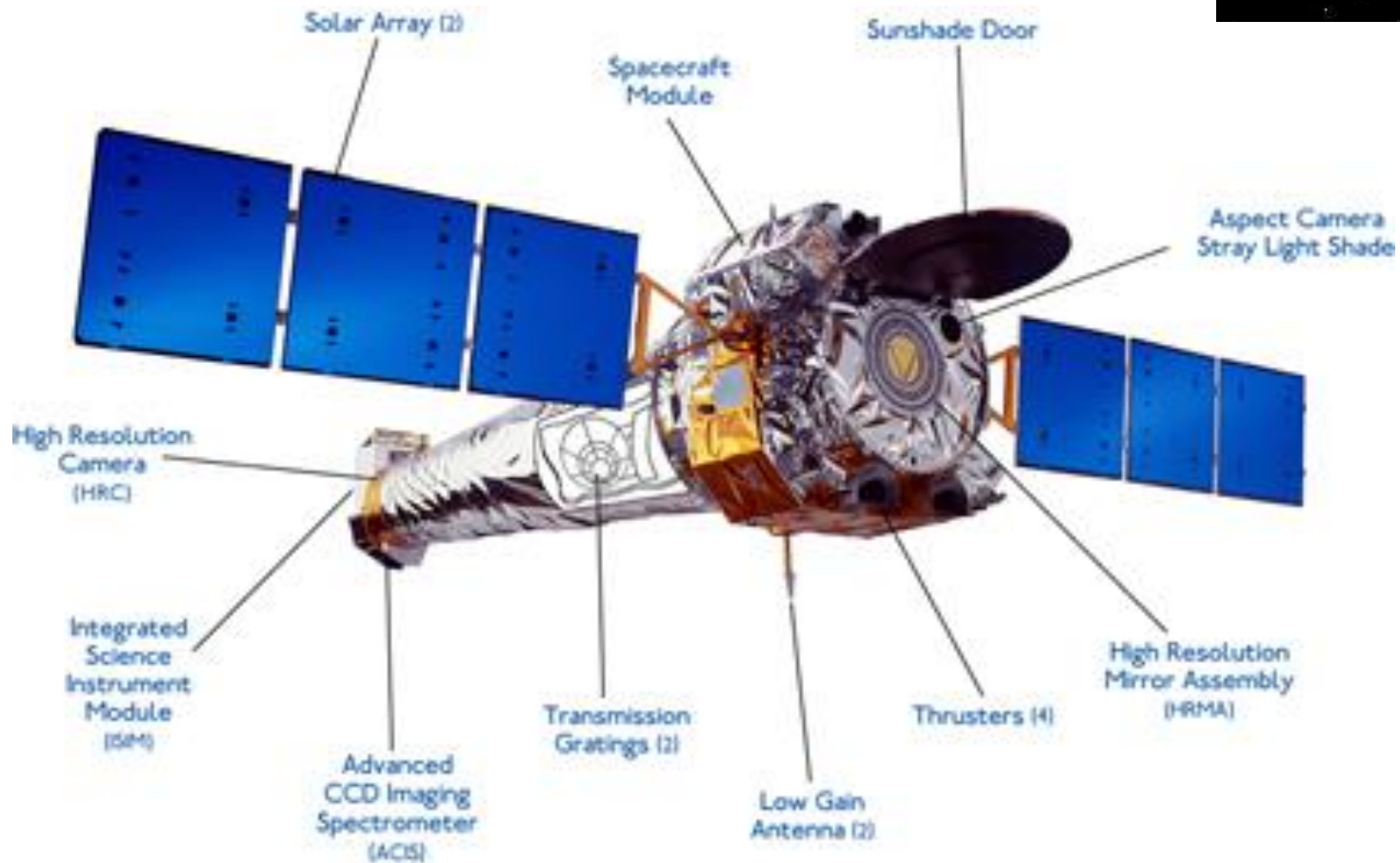
Target	ObsID	Starting Time (TT)	Usable Time (ks)	S/N	Telescope and Detector	Filter or Mode	Refs.
M28	2683	2002 Jul 4 18:02:19	14.0	23.85	<i>Chandra</i> ACIS-S3 (BI)	VFAINT	2
M28	2684	2002 Aug 4 23:46:25	13.9	23.54	<i>Chandra</i> ACIS-S3 (BI)	VFAINT	2
M28	2685	2002 Sep 9 16:55:03	14.3	23.90	<i>Chandra</i> ACIS-S3 (BI)	VFAINT	2
M28	9132	2008 Aug 7 20:45:43	144.4	78.75	<i>Chandra</i> ACIS-S3 (BI)	VFAINT	1, 3
M28	9133	2008 Aug 10 23:50:24	55.2	48.46	<i>Chandra</i> ACIS-S3 (BI)	VFAINT	1, 3
NGC 6397	79	2000 Jul 31 15:31:33	48.34	25.03	<i>Chandra</i> ACIS-I3 (FI)	FAINT	4, 5
NGC 6397	2668	2002 May 13 19:17:40	28.10	25.47	<i>Chandra</i> ACIS-S3 (BI)	FAINT	5
NGC 6397	2669	2002 May 15 18:53:27	26.66	24.97	<i>Chandra</i> ACIS-S3 (BI)	FAINT	5
NGC 6397	7460	2007 Jul 16 06:21:36	149.61	52.31	<i>Chandra</i> ACIS-S3 (BI)	VFAINT	5
NGC 6397	7461	2007 Jun 22 21:44:15	87.87	41.40	<i>Chandra</i> ACIS-S3 (BI)	VFAINT	5
M13	0085280301	2002 Jan 28 01:52:41	18.8	14.25	<i>XMM</i> pn, MOS1, MOS2	Medium	6, 7
M13	0085280801	2002 Jan 30 02:21:33	17.2	12.10	<i>XMM</i> pn, MOS1, MOS2	Medium	6, 7
M13	5436	2006 Mar 11 06:19:34	27.1	16.07	<i>Chandra</i> ACIS-S3 (BI)	FAINT	1, 8
M13	7290	2006 Mar 9 23:01:13	28.2	16.01	<i>Chandra</i> ACIS-S3 (BI)	FAINT	1, 8
ω Cen	653	2000 Jan 24 02:13:28	25.3	13.33	<i>Chandra</i> ACIS-I3 (FI)	VFAINT	9
ω Cen	1519	2000 Jan 25 04:32:36	44.1	16.45	<i>Chandra</i> ACIS-I3 (FI)	VFAINT	9
ω Cen	0112220101	2001 Aug 12 23:34:44	33.9	24.35	<i>XMM</i> pn, MOS1, MOS2	Medium	7, 10
NGC 6304	11074	2010 Jul 31 15:31:33	98.7	27.94	<i>Chandra</i> ACIS-I3 (FI)	VFAINT	1

Notes. TT refers to Terrestrial Time. FI and BI refers to the front-illuminated and back-illuminated ACIS chips.

References. (1) This work; (2) Becker et al. 2003; (3) Servillat et al. 2012; (4) Grindlay et al. 2001; (5) Guillot et al. 2011a; (6) Gendre et al. 2003b; (7) Webb & Barret 2007; (8) Catuneanu et al. 2013, (9) Rutledge et al. 2002; (10) Gendre et al. (2003a). All observations have been re-processed and re-analyzed in this work. The references provided here are given to indicate the previously published analyses of the data.

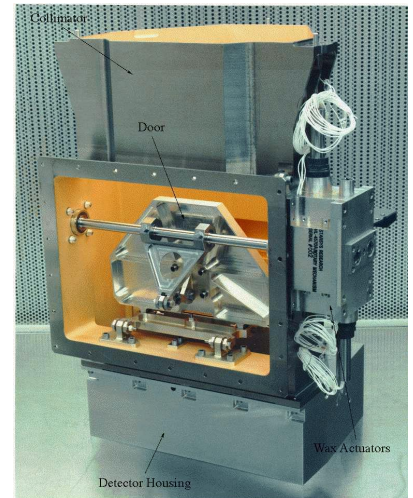
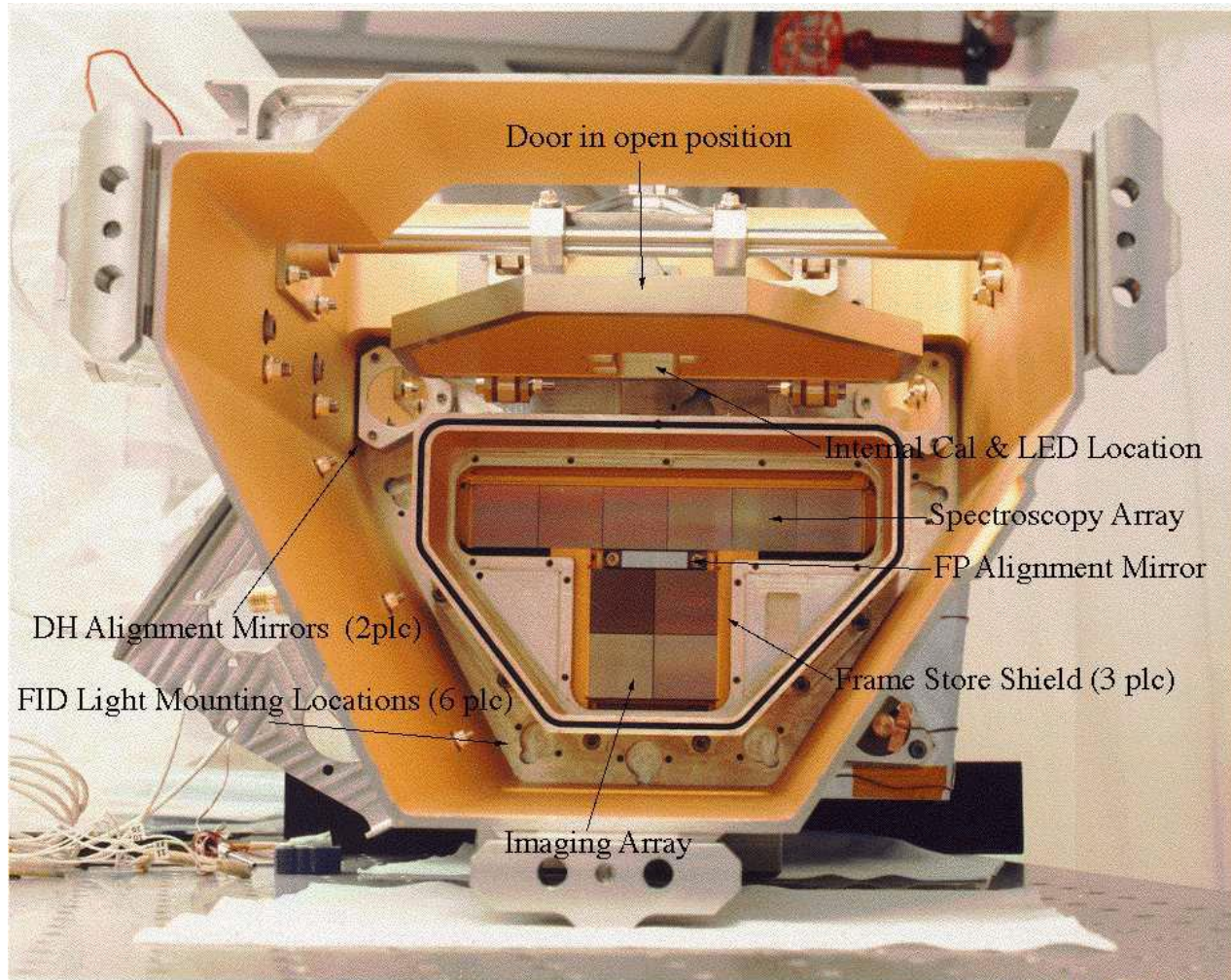
CHANDRA X-Ray Observatory

Launched 1999 (NASA)



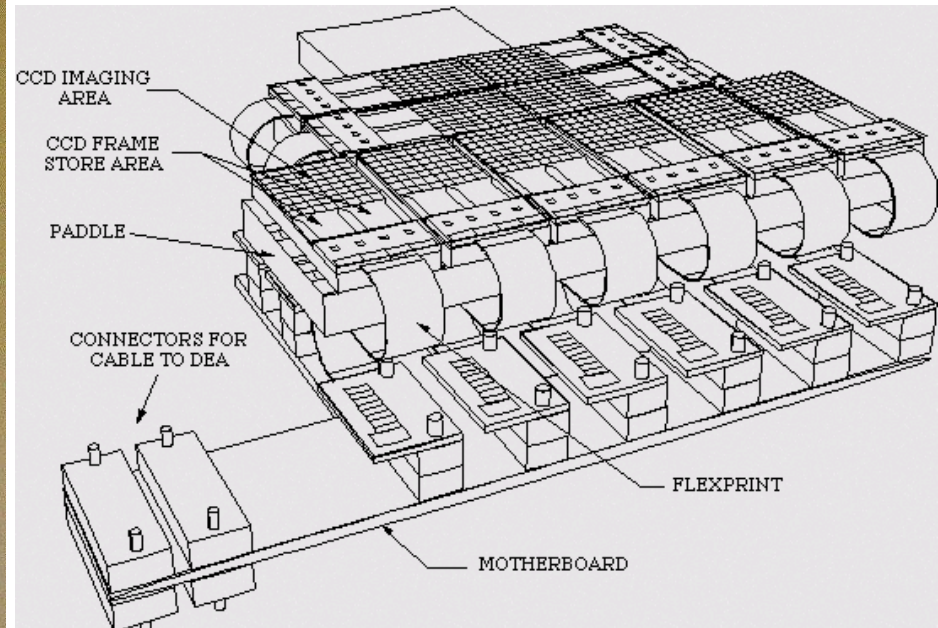
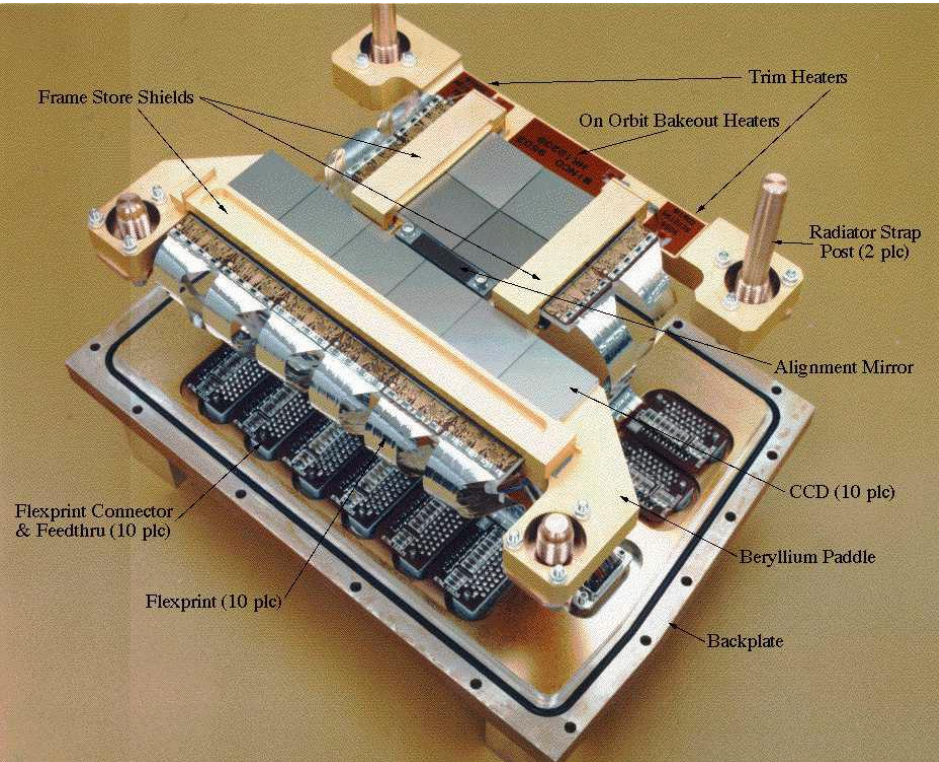
Advanced CCD Imaging Spectrometer

Developed at MIT and Pennsylvania State Univ.



Advanced CCD Imaging Spectrometer

3.24 sec/frame



XMM/Newton

Launched 1999 (European Space Agency)

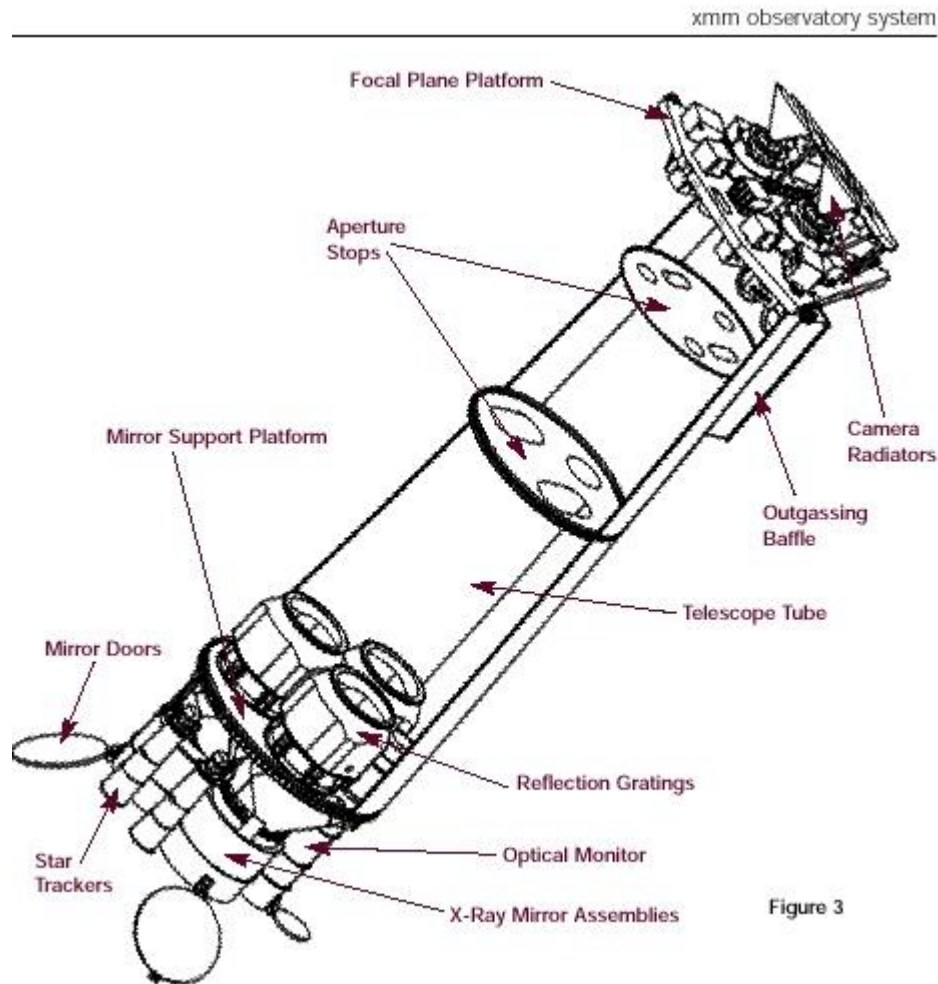


Figure 3



XMM/Newton Mirror

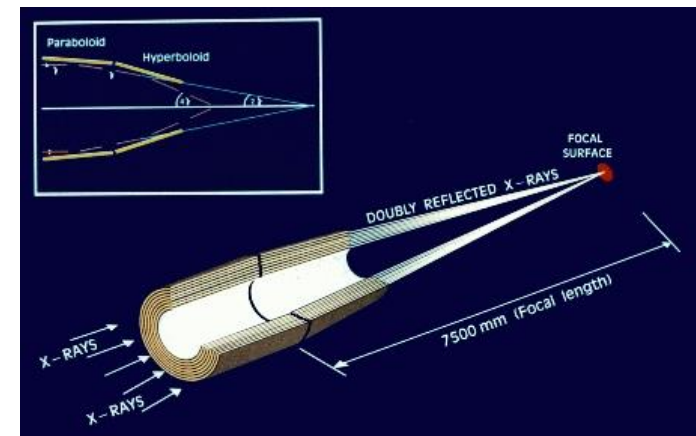
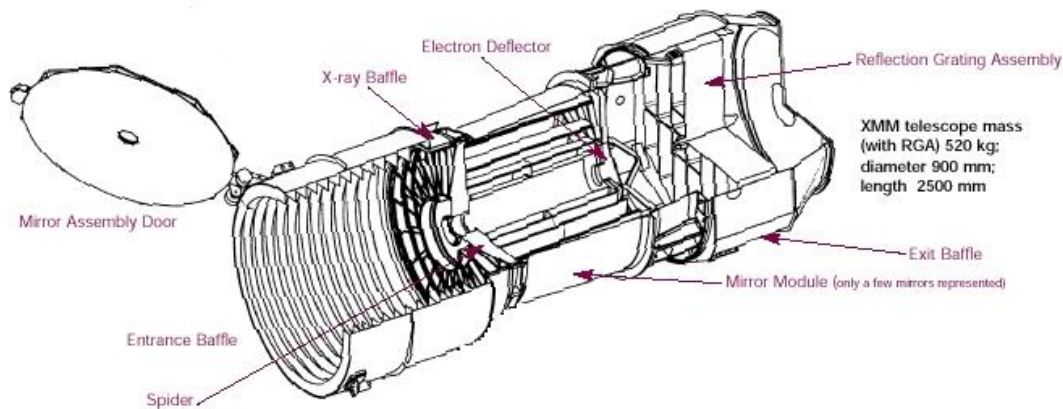
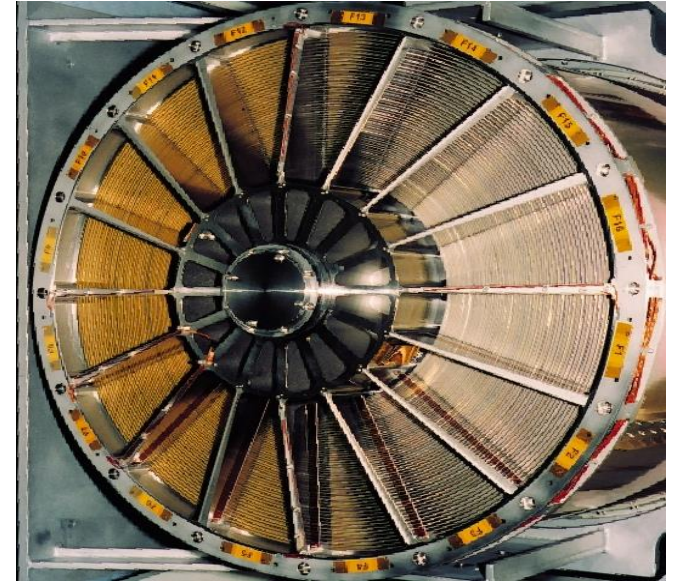
Wolter I grazing-incidence mirror

grazing angle: $30'$

focal length: 7.5 m

diameter: 70 cm

central photon energy: 7 keV



XMM/Newton X-Ray Detector

The European Photon Imaging Camera (EPIC)

Energy range from 0.15 to 15 keV

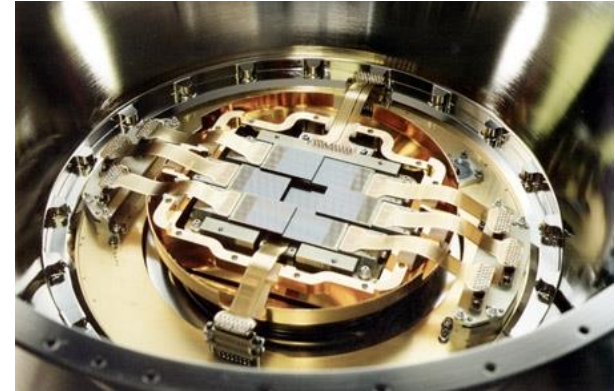
E/Delta E ~ 20-50

Angular resolution (PSF, 6 arcsec FWHM).

MOS CCD:

2.5 x 2.5 cm²

600 x 600, 40 μm-square pixels



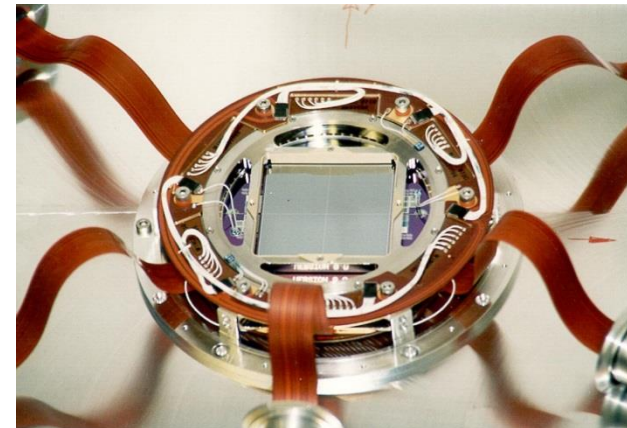
MOS Camera

pn CCD

6 x 6 cm²

150 x 150 μm²

73.4 msec/frame



pn Camera

Target qLMXB in Globular Clusters

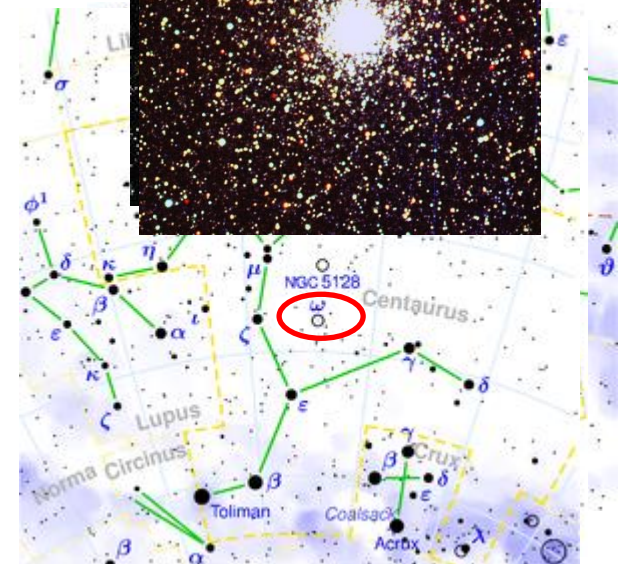
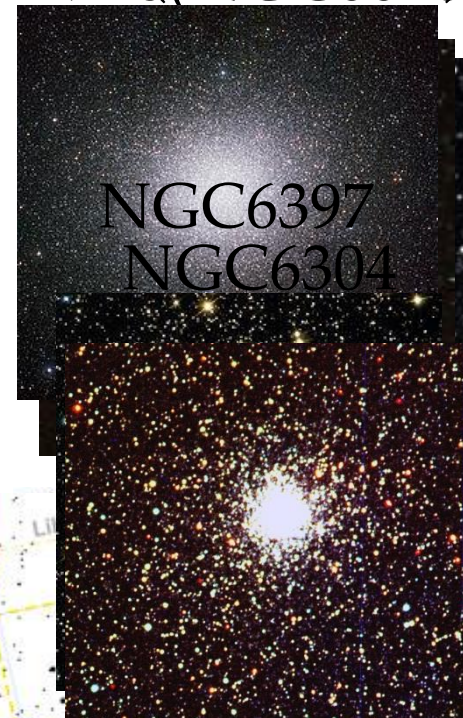
	distance (kpc)
• NGC6626(M28)	5.5 ± 0.3
• NGC6397	2.02 ± 0.18
• NGC6205(M13)	6.5 ± 0.6
• NGC5139(ω Cen)	4.8 ± 0.3
• NGC6304	6.22 ± 0.26

X7 in 47Tuc is excluded due to large pile-up.

Dynamical distance measurement (parallax) is possible for having well-understood uncertainty

HB (Horizontal Branch) is using the calibrated relation of RR Lyrae variables to estimate the

ω Cen(NGC5139)
M128(NGC6205)



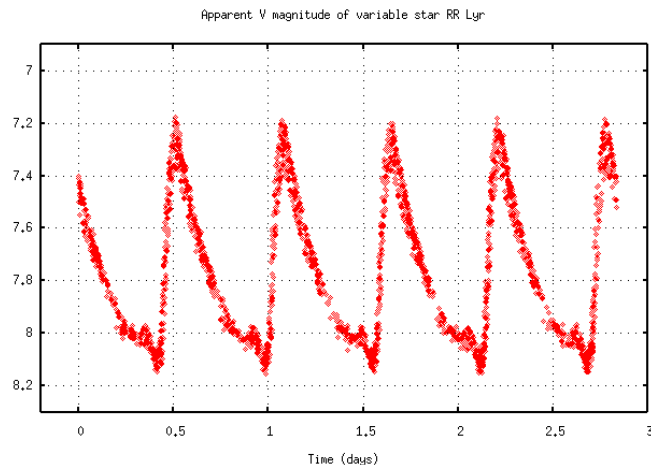
Globular Cluster Relevant Parameters

Table 3
Globular Cluster Relevant Parameters

Name	d_{GC} (kpc)	Method	$N_{H,22}$ (X-ray)	$N_{H,22}$ (H I)	Reference
M28	5.5 ± 0.3	Horizontal branch fitting	$0.256^{+0.024}_{-0.024}$	0.24	Testa et al. (2001)
NGC 6397	2.02 ± 0.18	Dynamical	$0.096^{+0.017}_{-0.014}$	0.14	Rees (1996)
M13	6.5 ± 0.6	Dynamical	$0.008^{+0.044}_{-0.007}$	0.011	Rees (1996)
ω Cen	4.8 ± 0.3	Dynamical	$0.182^{+0.045}_{-0.042}$	0.09	van de Ven et al. (2006)
NGC 6304	6.22 ± 0.26	Horizontal branch fitting	$0.346^{+0.105}_{-0.084}$	0.266	Recio-Blanco et al. (2005)

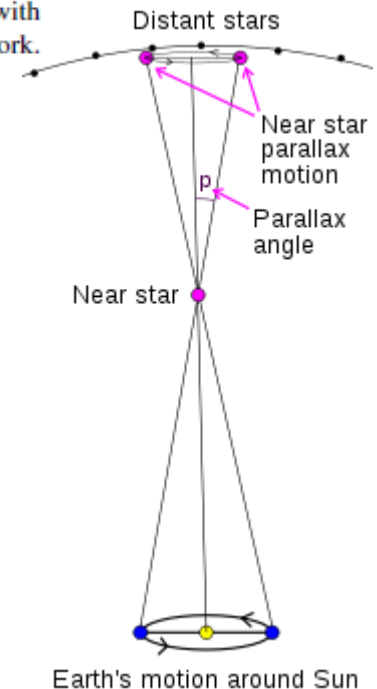
Notes. The selection of the distance values is described in Section 3.7, and the quoted uncertainties are 1σ . The N_H values are given in units of 10^{22} atoms cm^{-2} , with 90%-confidence uncertainties from X-ray spectral fitting. The N_H (H I) column corresponds to value in the direction of GCs, in the H I survey of (Dickey & Lockman 1990). The X-ray values are deduced from the best-fit N_H obtained from X-ray spectral fitting of each target in this work. Only the N_H values for NGC 6397 and ω Cen are not consistent with the H I values (see Section 4.1 for details). N_H values deduced from the present X-ray spectral analysis are used in the present work.

Horizontal branch (RR-Lyrae) using calibrated frequency-luminosity relation

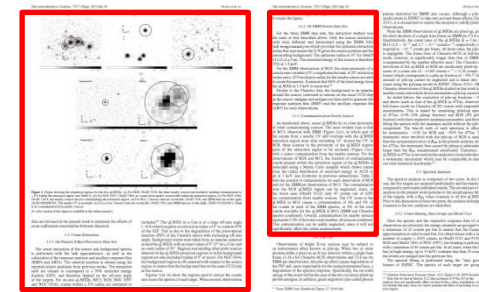
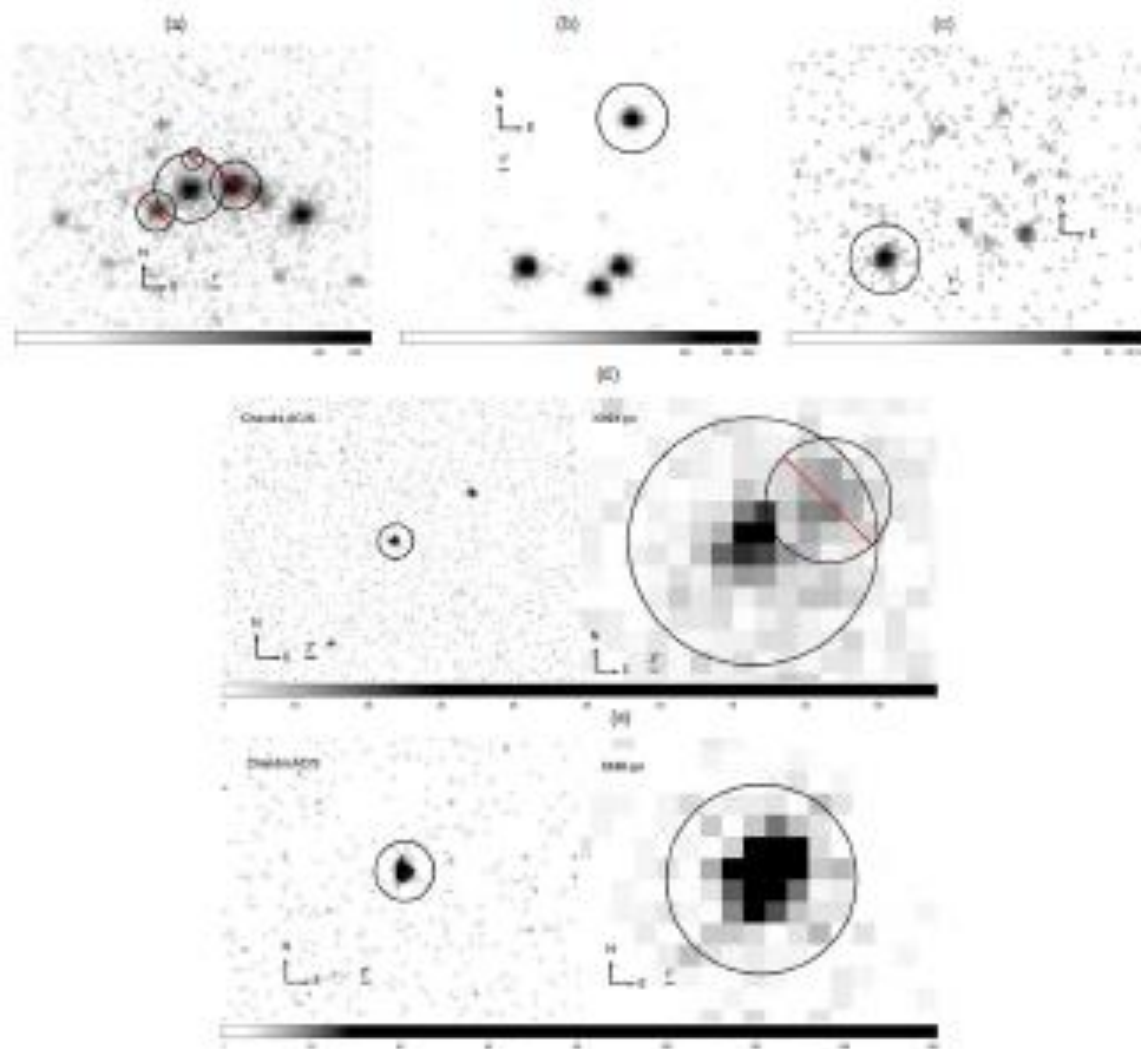


Originating from helium gas ionization, expansion and heat deposit oscillation

Dynamical Measurement (Parallax)



Counted regions and excluded regions



5

6

Count contamination from nearby sources (table-2) do not affect the result.

Figure 1. Figure showing the extraction regions for the five qLMXBs. (a) For M28, ObsID 9132, the three nearby sources are excluded, limiting contamination to $<1\%$ within the extraction region (see Table 2). (b) For NGC 6397, ObsID 7460, no counts from nearby sources fall within the extraction region. (c) For NGC 6304, ObsID 11074, the nearby sources are not contaminating the extraction region. (d) For M13, *Chandra* data are on the left, ObsID 7290, and *XMM* data are on the right, ObsID 0085280301. The nearby CV is excluded. (e) For ω Cen, *Chandra* data are on the left, ObsID 1519, and *XMM* data are on the right, ObsID 0112220101. There is no contamination from nearby sources.

(A color version of this figure is available in the online journal.)

Spectral Analysis

Emergent Spectrum of a Neutron Star Hydrogen Atmosphere

- H atmosphere calculated Spectra are ab initio radiative transfer calculations using the Eddington equations.

• Rajagopal and Romani (1996); Zavlin et al (1996); Pons et al (2002); Heinke et al (2006) – NSATMOS; Gaensicke, Braje & Romani (2001); Haakensen et al (2012)

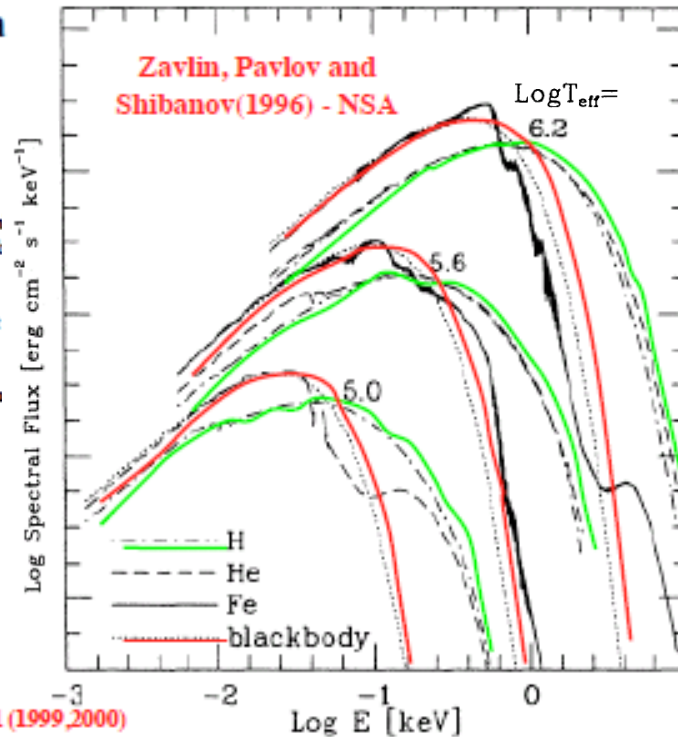
All comparisons show consistency within ~few % (e.g. Webb et 2007, Haakensen 2012).

“Vetted”: X-ray spectra of Zavlin, Heinke together have been used in several dozen works.

$$F = 4\pi T_{\text{eff},\infty}^4 \left(\frac{R_{\infty}}{D} \right)^2$$

$$R_{\infty} = \frac{R}{\sqrt{1 - \frac{2GM}{c^2 R}}}$$

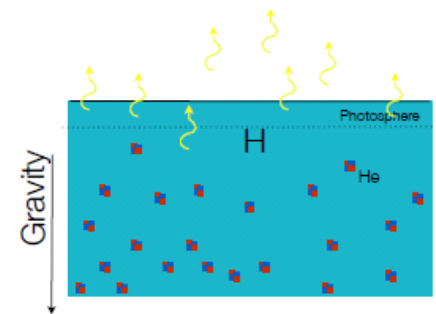
RR et al (1999,2000)



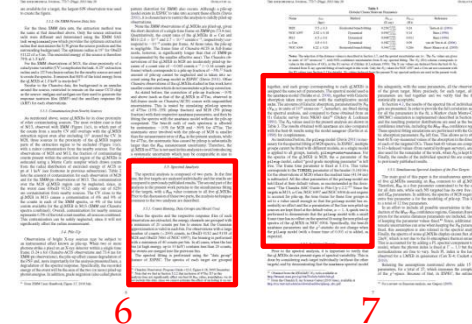
photon-e scattering and photon absorption

spectral model:
nsatmos

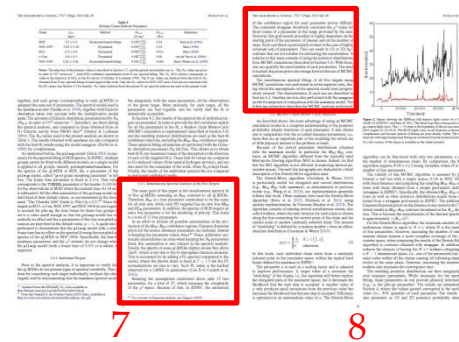
nsagrav is used to see model dependence



When accretion stops, the He and heavier elements gravitationally sink on a timescale of ~10s leaving the photosphere to be pure hydrogen (Alcock & Illarionov 1980 Bildsten et al., 1992)



Free Parameters to Fit



- R_{NS} : NS Radius, common for all the five qLMXBs
- T_{eff} : NS effective temperature $\times 5$
- M_{NS} : NS mass $\times 5$
- α : pile-up parameter for M28
- $:$: prior source distance (Gaussian shape) $\times 5$
- N_H : galactic absorption normalization $\times 5$
- $:$: power law (PL) index for hard spectral component $\times 5$

Galactic Absorption Parameter N_H

Galactic Survey:

National Radio Astronomy Observatory (NRAO)

<https://science.nrao.edu/>

[Dickey and Lockmann Ann. Rev. Astron. Astrophys.28, 215\(1990\)](#)

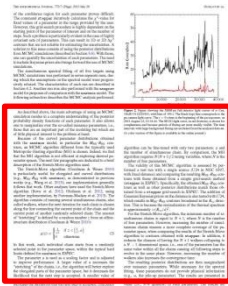
N_{HI} : Neutral Hydrogen Atom Column Density

N_{H_2} : Hydrogen Molecule Column Density

N_{HI} data are not used in the analysis of G13,
but N_H are fitted as free parameters.



Statistical Method



Markov Chain Monte-Carlo Analysis (using *Stretch-Move* algorithm):

A kind of Monte-Carlo analysis for making Bayesian reasoning.

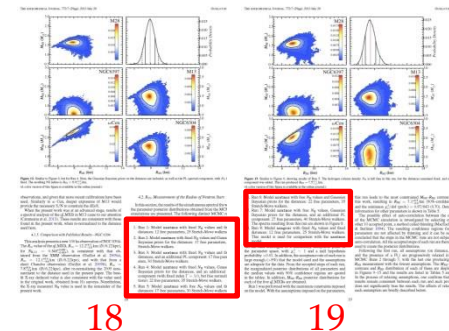
Markov Chain: a chain of steps where the next step is determined only by the information in the previous step.

Several simultaneous chains with the weight function determined by the likelihood function in the previous chains and random numbers.

Advantage: complete understanding of the posterior probability density functions (uncertainties) of each parameters.

Simulation Conditions (Runs)

1. Run 1: Model `nsatmos` with fixed N_H values and fixed distances: 12 free parameters, 25 Stretch-Move walkers.
2. Run 2: Model `nsatmos` with fixed N_H values and Gaussian Bayesian priors for the distances: 17 free parameters, 30 Stretch-Move walkers.
3. Run 3: Model `nsatmos` with fixed N_H values and fixed distances, and an additional PL component: 17 free parameters, 30 Stretch-Move walkers.
4. Run 4: Model `nsatmos` with fixed N_H values, Gaussian Bayesian priors for the distances, and an additional PL component (with fixed index $\Gamma = 1.0$, but free normalizations): 22 free parameters, 35 Stretch-Move walkers.
5. Run 5: Model `nsatmos` with free N_H values and fixed distances: 17 free parameters, 30 Stretch-Move walkers.
6. Run 6: Model `nsatmos` with free N_H values and Gaussian Bayesian priors for the distances: 22 free parameters, 35 Stretch-Move walkers.
7. Run 7: Model `nsatmos` with free N_H values, Gaussian Bayesian priors for the distances, and an additional PL component: 27 free parameters, 40 Stretch-Move walkers. The spectra resulting from this run are shown in Figure 8.
8. Run 8: Model `nsagrav` with fixed N_H values and fixed distances: 12 free parameters, 25 Stretch-Move walkers. This model is used for comparison with the `nsatmos` model.



Step by step simulations with relaxing fixed parameters.

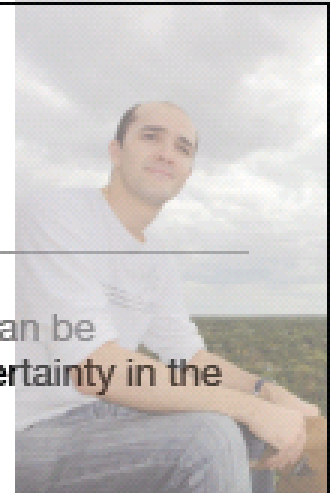
Assumptions -- the systematic uncertainties.

- **H atmosphere neutron stars.** (expected from a Hydrogen companion LMXB; can be proven through optical observations with Hubble, only done in one case, Omega Cen).
- **Low B-field ($<10^{10}$ G) neutron stars.** (this is true for 'standard' LMXBs as a class, but difficult to prove on a case-by-case basis).
- **Emitting isotropically.** (comes naturally when powered by a hot core).

These assumptions reflect the best knowledge of these systems astronomy has in 2013.
If you don't like these assumptions: "We find the assumptions not strongly supported
and therefore ignore this result."

Accounted-for Uncertainties

- In all previous works using qLMXB, the distance uncertainty -- which can be 2%-10% for each source -- has been neglected. **Reflected in the uncertainty in the measured radius.**
- X-ray absorption (due to the Hydrogen column density) is sometimes held fixed at radio-measured values, but is known to be systematically uncertain by $\times 2$, unless measured in the X-ray band. **Reflected in the uncertainty in the measured radius.**
- In some field sources (but no globular cluster sources) excess emission at high energies, not due to a H atmosphere, has been detected. **Reflected in the uncertainty in the measured radius.**
- Calibration uncertainty is included as a 3% intensity uncertainty.
- There are no remaining known quantified uncertainties.



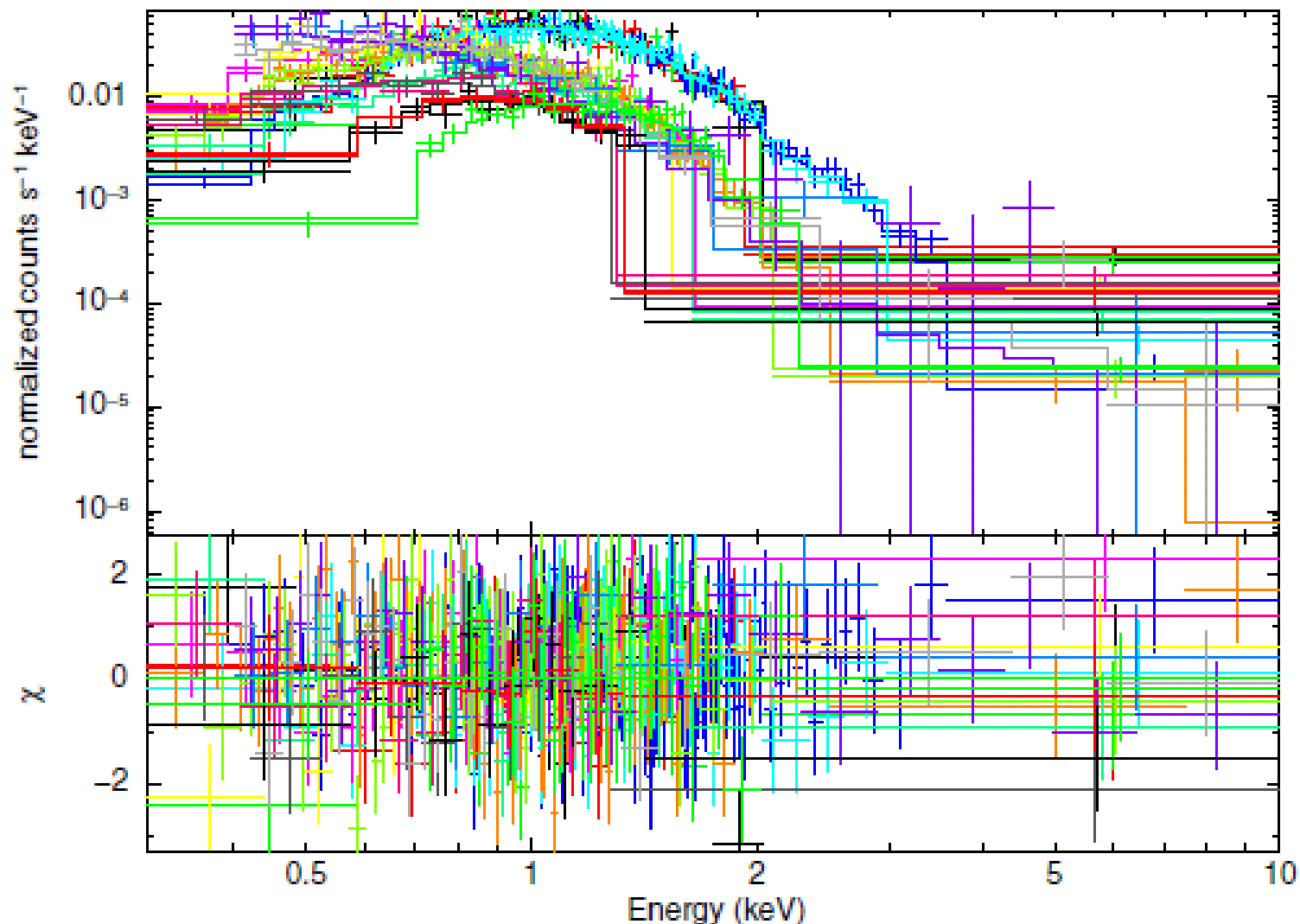
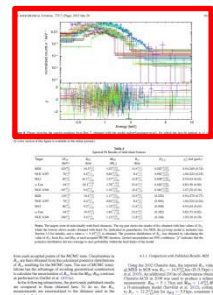
The major innovation of Guillot et al (2013) is statistical.

- All work to date, in combining spectral fits, fit each source individually, then combined the best fit M and R afterwards, with error regions.
- Guillot et al (2013) required R to be the same for all sources.
- This “quasi-constant Radius” should be thought of as a simplified parametric model which can be compared to realistic EoSs.
- The result is an improvement in S/N over previous work which (for example) would use 5 sources independently, (approximately) as if we had 25 sources.
- A simplified explanation.....

Results

Pages 13-21

Results



14

Figure 8. Figure showing the spectra resulting from Run 7, obtained with the model `wabs*(nsatmos+pow)`, for which the best-fit statistic is χ^2_{ν}/dof (prob.) = 0.98/628 (0.64).

(A color version of this figure is available in the online journal.)

Results

Table 6
Results from the Simultaneous Spectral Fitting, with Free N_H

Target	α_{pileup}	kT_{eff} (eV)	M_{NS} (M_{\odot})	R_{∞} (km)	$N_{\text{H},22}$	PL Norm $\times 10^{-7}$ ($\text{keV}^{-1} \text{s}^{-1} \text{cm}^{-2}$)
M28	$0.43^{+0.13}_{-0.13}$	165^{+24}_{-22}	$1.60^{+0.21}_{-0.25}$	$12.4^{+1.6}_{-1.5}$	$0.248^{+0.023}_{-0.022}$...
NGC 6397	...	70^{+8}_{-5}	$0.76^{+0.33}_{-0.22p}$	$9.0^{+1.4}_{-1.1}$	$0.105^{+0.016}_{-0.015}$...
M13	...	106^{+20}_{-16}	$1.43^{+0.36}_{-0.44p}$	$11.4^{+2.5}_{-1.7}$	$0.010^{+0.024}_{-0.009p}$...
ω Cen	...	137^{+32}_{-31}	$2.00^{+0.36}_{-0.41}$	$16.7^{+4.7}_{-4.3}$	$0.152^{+0.048}_{-0.049}$...
NGC 6304	...	120^{+28}_{-14}	$1.13^{+0.59}_{-0.54p}$	$10.1^{+3.2}_{-1.9}$	$0.315^{+0.079}_{-0.060}$...

24

Run 5: Free N_H , Fixed d_{GC} , No PL included, $R_{\text{NS}} = 7.5^{+1.1}_{-1.0}$ km

χ^2_{ν}/dof (prob.) = 0.98/638 (0.66), 8% accept. rate

M28	$0.43^{+0.13}_{-0.13}$	165^{+24}_{-22}	$1.60^{+0.21}_{-0.25}$	$12.4^{+1.6}_{-1.5}$	$0.248^{+0.023}_{-0.022}$...
NGC 6397	...	70^{+8}_{-5}	$0.76^{+0.33}_{-0.22p}$	$9.0^{+1.4}_{-1.1}$	$0.105^{+0.016}_{-0.015}$...
M13	...	106^{+20}_{-16}	$1.43^{+0.36}_{-0.44p}$	$11.4^{+2.5}_{-1.7}$	$0.010^{+0.024}_{-0.009p}$...
ω Cen	...	137^{+32}_{-31}	$2.00^{+0.36}_{-0.41}$	$16.7^{+4.7}_{-4.3}$	$0.152^{+0.048}_{-0.049}$...
NGC 6304	...	120^{+28}_{-14}	$1.13^{+0.59}_{-0.54p}$	$10.1^{+3.2}_{-1.9}$	$0.315^{+0.079}_{-0.060}$...

Run 6: Free N_H , Gaussian Bayesian priors for d_{GC} , No PL included, $R_{\text{NS}} = 7.8^{+1.3}_{-1.1}$ km

χ^2_{ν}/dof (prob.) = 0.99/633 (0.59), 8% accept. rate

M28	$0.42^{+0.13}_{-0.13}$	158^{+26}_{-29}	$1.59^{+0.25}_{-0.45p}$	$12.4^{+1.8}_{-1.7}$	$0.248^{+0.023}_{-0.022}$...
NGC 6397	...	71^{+9}_{-5}	$0.78^{+0.39}_{-0.24p}$	$9.4^{+1.6}_{-1.3}$	$0.104^{+0.016}_{-0.015}$...
M13	...	100^{+23}_{-18}	$1.38^{+0.42}_{-0.64p}$	$11.3^{+2.6}_{-2.0}$	$0.010^{+0.023}_{-0.009p}$...
ω Cen	...	133^{+35}_{-30}	$2.07^{+0.41p}_{-0.43}$	$17.1^{+5.2}_{-4.4}$	$0.156^{+0.050}_{-0.048}$...
NGC 6304	...	116^{+30}_{-14}	$1.09^{+0.68}_{-0.52p}$	$10.3^{+3.4}_{-1.9}$	$0.321^{+0.078}_{-0.061}$...

Run 7: Free N_H , Gaussian Bayesian priors for d_{GC} , PL included, $R_{\text{NS}} = 9.1^{+1.3}_{-1.5}$ km

χ^2_{ν}/dof (prob.) = 0.98/628 (0.64), 7% accept. rate

M28	$0.34^{+0.14}_{-0.14}$	137^{+29}_{-22}	$1.50^{+0.37}_{-0.80p}$	$12.6^{+2.0}_{-2.0}$	$0.248^{+0.024}_{-0.023}$	$5.0^{+3.7}_{-3.4p}$
NGC 6397	...	67^{+8}_{-5}	$0.86^{+0.47}_{-0.31p}$	$10.8^{+1.7}_{-1.7}$	$0.116^{+0.017}_{-0.017}$	$2.7^{+1.3}_{-1.3}$
M13	...	92^{+24}_{-15}	$1.47^{+0.62}_{-0.78p}$	$12.6^{+3.7}_{-2.3}$	$0.014^{+0.028}_{-0.012p}$	$2.4^{+4.1}_{-2.1p}$
ω Cen	...	130^{+33}_{-31}	$2.42^{+0.42p}_{-0.54}$	$20.3^{+5.6}_{-5.7}$	$0.172^{+0.047}_{-0.051}$	$2.9^{+3.9}_{-2.6p}$
NGC 6304	...	112^{+31}_{-15}	$1.32^{+0.80}_{-0.71p}$	$12.1^{+4.3}_{-2.5}$	$0.346^{+0.086}_{-0.065}$	$1.8^{+2.6}_{-1.5p}$

Results

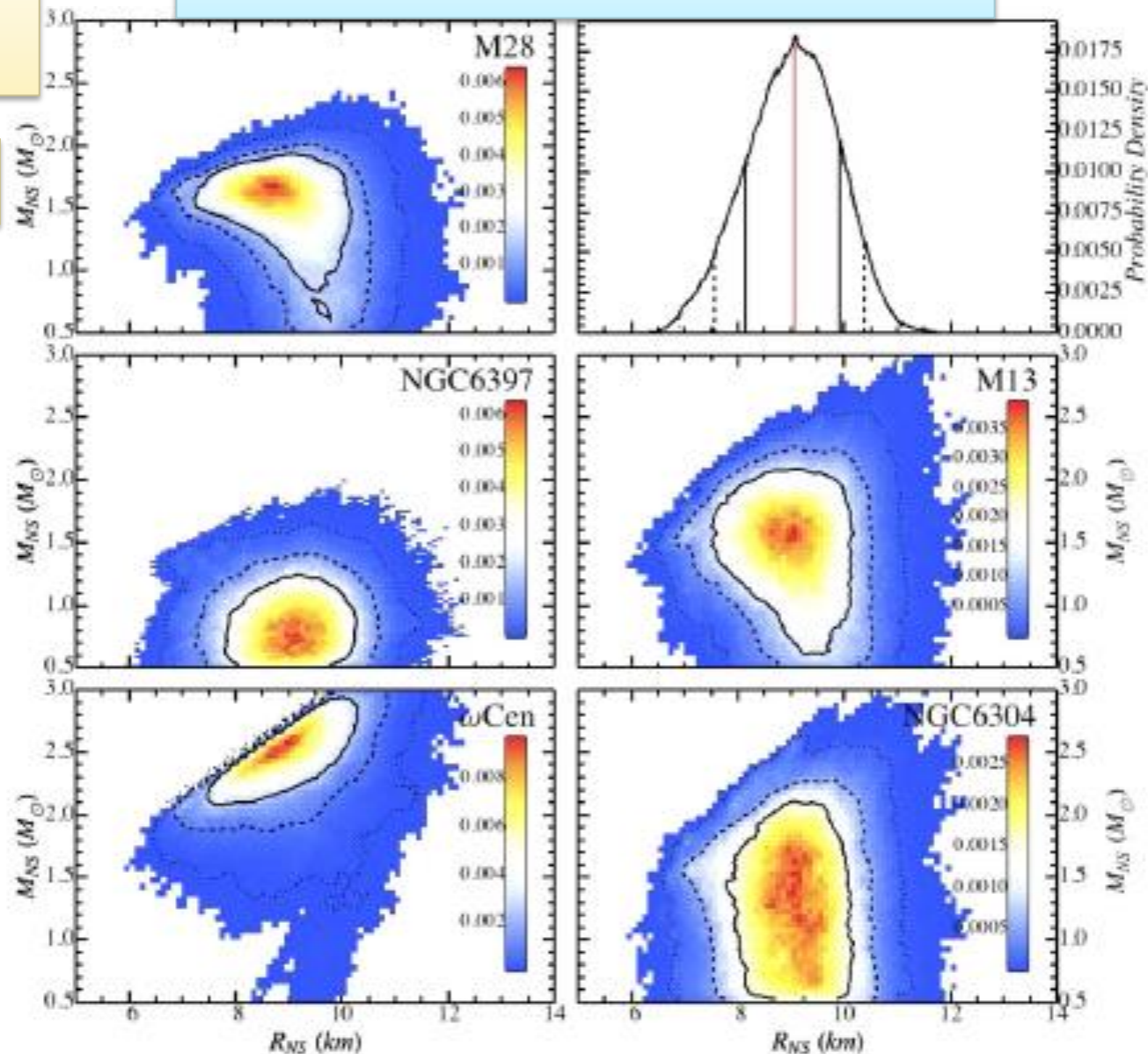
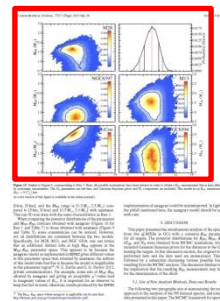


Figure 15. Similar to Figure 9, corresponding to Run 7. Here, all possible assumptions have been relaxed in order to obtain a R_{NS} measurement that is least affected by systematic uncertainties. The N_{IT} parameters are left free; and Gaussian Bayesian priors and PL components are included. This results in an R_{NS} measurement: $R_{\text{NS}} = 9.1^{+1.3}_{-1.5}$ km.

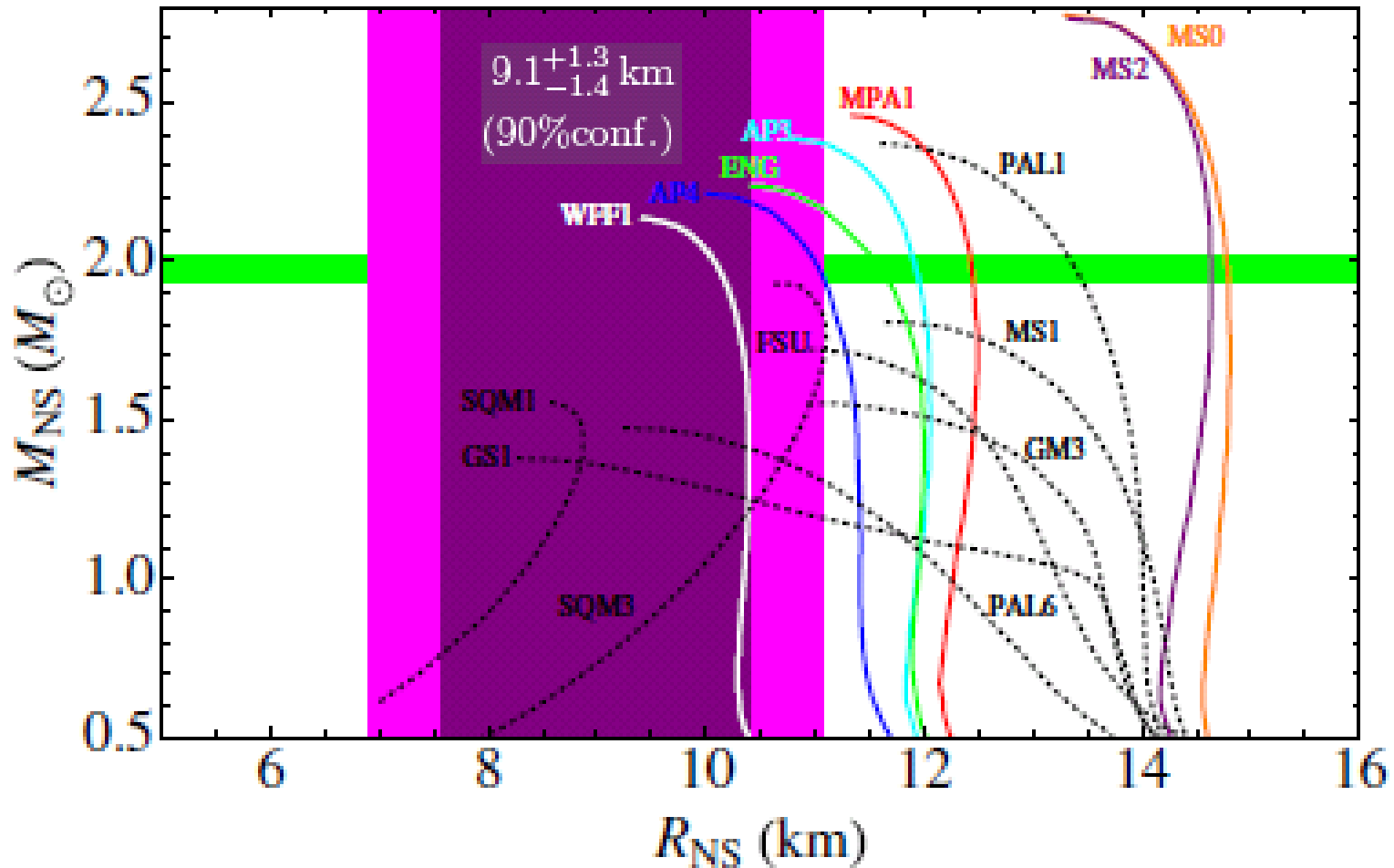
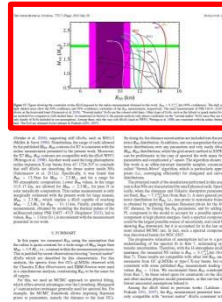
(A color version of this figure is available in the online journal.)



Discussion

Pages 21-27

Neutron Star Radius

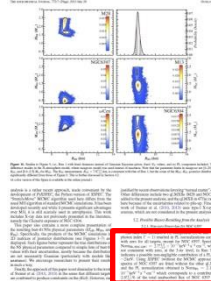


27

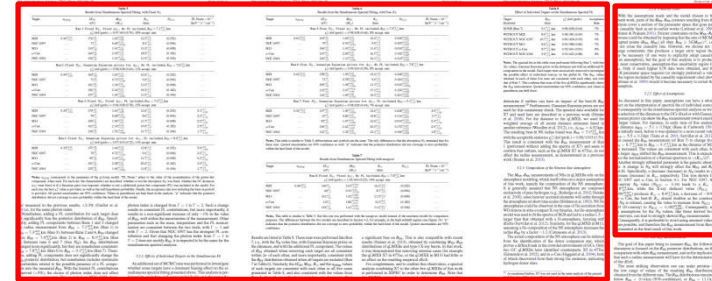
Figure 17. Figure showing the constraint on the dEoS imposed by the radius measurement obtained in this work: $R_{\text{NS}} = 9.1^{+1.3}_{-1.5}$ km (90%-confidence). The dark and light shaded areas show the 90%-confidence and 99%-confidence constraints of the R_{NS} measurement, respectively. The mass measurement of PSR J1614–2230 is shown as the horizontal band (Demorest et al. 2010). “Normal matter” EoSs are the colored solid lines. Other types of EoSs, such as the hybrid or quark-matter EoSs are included for comparison, with dashed lines. As mentioned in Section 5, the present analysis only places constraints on the “normal matter” EoSs since they are the only family of EoSs included in our assumptions. Among them, only the very soft dEoSs (such as WFF1; Wiringa et al. 1988) are consistent with the radius obtained here. The EoS are obtained from Lattimer & Prakash (2001, 2007).

(A color version of this figure is available in the online journal.)

Possible Biases



24



25

26

27

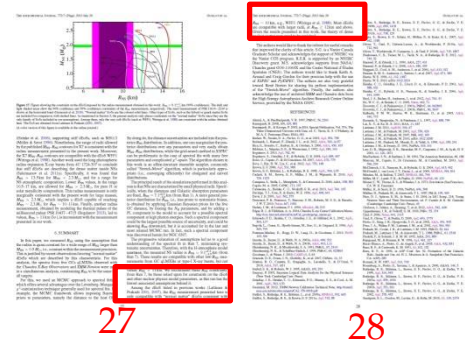
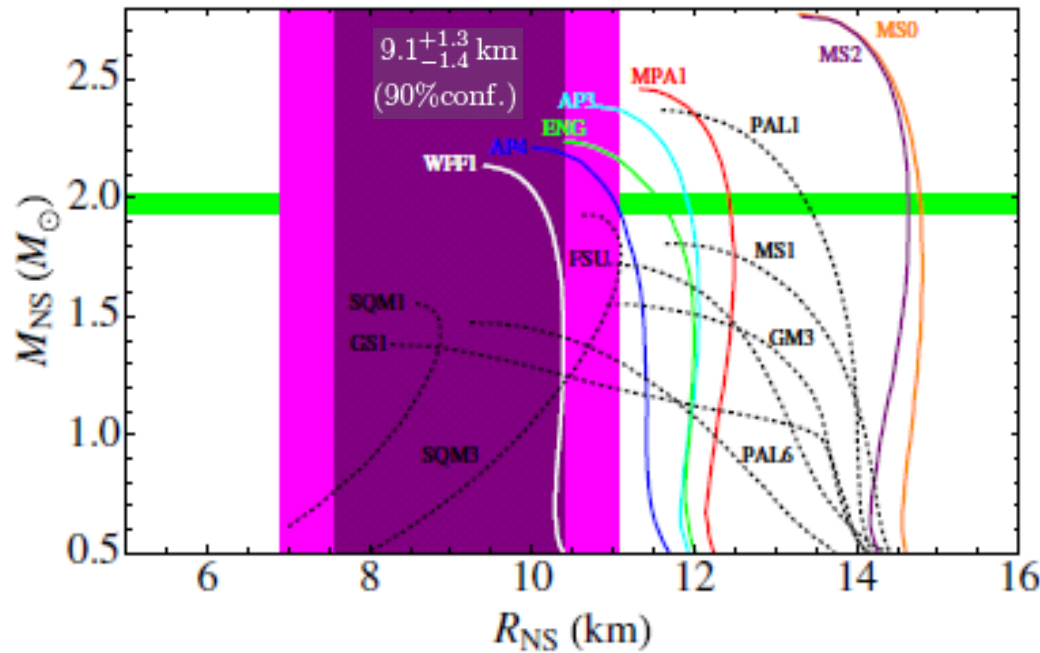
1. None-zero power-law component for NGC6397 (all other PL values are zero).
2. Effect of individual targets on the simultaneous fit
3. Composition of the NS atmosphere
4. Causality limit
5. Effect of assumptions
 1. distances (fixed or Gaussian prior)
 2. galactic absorption (N_H)

This is not important for finding the most probable R_{NS} radius.

This may affect the result. Only for X5 in 47Tuc and ω Cen, composition of the companion star is identified and that is hydrogen.

Strongly skewed R_{NS} is obtained when H_I survey values are assumed.

Summary



The R_{NS} measurement presented here is only compatible with “normal matter” dEOS consistent with $R_{\text{NS}} \sim 10$ km e.g. WFF1.

Given the results presented in this work, the theory of dense nuclear matter need to be revisited.

LS13

Neutron Star Masses and Radii from Quiescent Low-Mass X-ray Binaries

James M. Lattimer

*Department of Physics and Astronomy, State University of New York at Stony Brook, Stony Brook, NY
11794-3800, USA*

james.lattimer@stonybrook.edu

Andrew W. Steiner

Institute for Nuclear Theory, University of Washington, Seattle, WA 98195, USA

steiner3@uw.edu

ABSTRACT

A recent analysis (Guillot et al. 2013) of the thermal spectra of 5 quiescent low-mass X-ray binaries in globular clusters, in which it was assumed that all neutron stars have the same radius, determined the radius to be $R = 9.1_{-1.5}^{+1.3}$ km to 90% confidence. However, the masses of the sources were found to range from $0.86 M_{\odot}$ to $2.4 M_{\odot}$ and a significant amount of the predicted $M - R$ region violates causality and the existence of a 2 solar mass neutron star. The study determined the amount of Galactic absorption along the lines-of-sight from fitting the X-ray spectra and assumed all sources possessed hydrogen atmospheres. We argue, from a Bayesian analysis, that different interpretations of the data are strongly favored. Our most-favored model assumes i) the equation of state of neutron star crusts is well-understood, ii) the high-density equation of state is consistent with causality and the existence of neutron stars at least as massive as $2 M_{\odot}$, iii) that the Galactic absorption is determined either from the fits in Guillot et al. (2013) or from independent HI surveys, and iv) that these objects are well-described by either hydrogen or helium atmospheres. With these assumptions, the 90% confidence radius range for $1.4 M_{\odot}$ stars is 11.4 to 12.8 km, and the allowed range for radii of all neutron stars between $1.2 M_{\odot}$ and $2.0 M_{\odot}$ is 10.9 to 12.7 km. This result is in much greater agreement with predictions of the equation of state from both nuclear experiments and theoretical neutron matter studies than the smaller radii deduced by Guillot et al. (2013).

Strong objection to G13!

LS13: Objections

1. The mass in the G13 result is range from $0.86 - 2.4 M_{\odot}$, violating the causality limit and the existence of $2 M_{\odot}$ NSs.
2. G13 takes N_H 's as free parameters to fit the spectra instead of using the independent N_H -survey data.
3. G13 assumes hydrogen atmosphere.

LS13: Claims

Our most-favored method assumes

1. The equation of state of neutron star crusts is well-understood.
2. The high-density equation of state is consistent with causality and the existence of neutron stars at least as massive as $2 M_{\odot}$.
3. The Galactic absorption is determined either from the fits in G13 or from independent H_I surveys
4. These objects are well-described by either hydrogen or helium atmospheres.

With these assumptions, the 90% confidence radius range is
11.4 to 12.8 km for $1.4 M_{\odot}$
10.9 to 12.7 km for $1.2\text{-}2.0 M_{\odot}$

This result is in much greater agreement with predictions of the equation of state from both nuclear experiments and theoretical neutron matter studies than the smaller radii deduced by G13.

LS13: Assumptions

1. Adapted a scale on the N_H dependence to the G13 results in order to apply the N_H -survey result (“alternative”)
2. Adapted an approximated analytical dependence on the atmosphere to the G13 results in order to discuss the atmosphere dependence. (H or H+He)
3. Adapted a dependence on gravity and red-shift to the G13 results.
4. Assumed three kinds of parameterized EOS:
 - “baseline”: normal matter
 - “exotic”: strong phase transition at high density (e.g. quark-hadron phase transition)

LS13: Results

Likelihood Function

TABLE 4
PROPERTIES THE BAYESIAN MODELS

Model	M (M_{\odot})	R (km)	R_{∞} (km)	z	I
Base	1.31 ± 0.40	11.09 ± 0.39	13.8 ± 1.1	0.25 ± 0.12	$(7.32 \pm 0.37) \times 10^{-9}$
Exo	1.31 ± 0.43	9.68 ± 0.64	12.6 ± 1.8	0.31 ± 0.16	$(9.60 \pm 0.57) \times 10^{-6}$
Alt	1.17 ± 0.26	11.02 ± 0.33	13.2 ± 0.7	0.21 ± 0.07	$(5.83 \pm 0.36) \times 10^{-3}$
Exo/Alt	1.17 ± 0.26	9.81 ± 0.44	12.1 ± 0.9	0.25 ± 0.08	$(8.19 \pm 1.35) \times 10^{-1}$
H+He	1.42 ± 0.41	11.21 ± 0.76	15.0 ± 1.3	0.25 ± 0.11	$(1.46 \pm 0.08) \times 10^{-3}$
Exo/H+He	1.47 ± 0.51	11.24 ± 0.55	14.5 ± 2.1	0.29 ± 0.15	$(5.58 \pm 0.39) \times 10^{-2}$
Alt/H+He	1.34 ± 0.31	12.02 ± 0.58	14.6 ± 0.8	0.23 ± 0.09	$(1.55 \pm 0.06) \times 10^{+2}$
Alt/Exo/H+He	1.34 ± 0.33	11.48 ± 0.68	14.1 ± 1.2	0.24 ± 0.09	$(1.84 \pm 0.07) \times 10^{+1}$

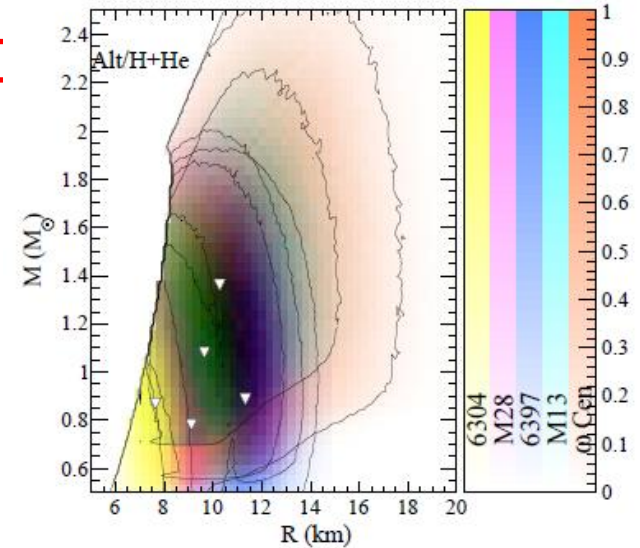
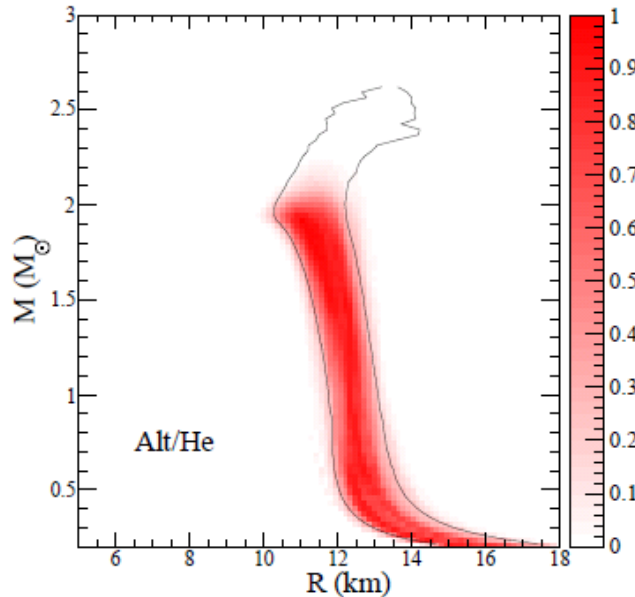


Fig. 5.— Probability distributions in the (z, R_{∞}) and (M, R) planes assuming the adjusted N_H value, but allowing the composition of the atmosphere to be either hydrogen or helium. A black and white version is given in an Appendix at the end.

Objections to LS13

LSI 3:

How it should be done.

- Download all X-ray data from the NASA Archive heasarc.gsfc.nasa.gov. All observations are freely available, as are all standard analysis tools. This is done 1000s of times every year by astronomers and results in 1000s of papers annually. That said, it is not idiot-proof.
- Extract X-ray photon spectra from each source. (Hereafter: “Data” means “X-ray photon spectra”, and nothing else.)
- Perform a (for example) Chi-square minimization (or other figure of merit) comparison between the proposed photon spectral model and the X-ray photon spectral data. Is the chi-square “acceptable”? Is it “better” than alternative models?

LS 13:

What is actually done

- LS13 gives the impression that our group gave them photon spectral data. **We did not.** We provided numeric values for our best (M,R,T,NH) fits to each source, and their error regions -- which anyone could read from figures in our papers.
- LS13 uses an (unpublished) semi-analytic model for the spectrum (A minor issue: why not use the heavily vetted and widely distributed models NSATMOS (Heinke 2006) or NSA (Zavlin et al 1996)?)
- Normalizes this model against G13 best-fit values and uncertainties, and then compares a Bayesian likelihood of this best fit model to an extrapolated model using different assumptions applied to their analytic model.
- LS13 is not “data analysis” in any sense at all. This is “data modeling theory”. It answers the question: **“If the data look like our model, this is what the results would be.”**. Also: **“If someone were to do our analysis with the data, and the data are described by our analytic model, then this is what the results would be.”** **It does not say what the data are actually saying.**

TABLE 4
PROPERTIES THE BAYESIAN MODELS

Model	$M (M_{\odot})$	R (km)	R_{∞} (km)	z	I (Figure of merit)
Base	1.31 ± 0.40	11.09 ± 0.39	13.8 ± 1.1	0.25 ± 0.12	$(7.32 \pm 0.37) \times 10^{-9}$
Exo	1.31 ± 0.43	9.68 ± 0.64	12.6 ± 1.8	0.31 ± 0.16	$(9.60 \pm 0.57) \times 10^{-6}$
Alt	1.17 ± 0.26	11.02 ± 0.33	13.2 ± 0.7	0.21 ± 0.07	$(5.83 \pm 0.36) \times 10^{-3}$
Exo/Alt	1.17 ± 0.26	9.81 ± 0.44	12.1 ± 0.9	0.25 ± 0.08	$(8.19 \pm 1.35) \times 10^{-1}$
H+He	1.42 ± 0.41	11.21 ± 0.76	15.0 ± 1.3	0.25 ± 0.11	$(1.46 \pm 0.08) \times 10^{-3}$
Exo/H+He	1.47 ± 0.51	11.24 ± 0.55	14.5 ± 2.1	0.29 ± 0.15	$(5.58 \pm 0.39) \times 10^{-2}$
Alt/H+He	1.34 ± 0.31	12.02 ± 0.58	14.6 ± 0.8	0.23 ± 0.09	$(1.55 \pm 0.06) \times 10^{+2}$
Alt/Exo/H+He	1.34 ± 0.33	11.48 ± 0.68	14.1 ± 1.2	0.24 ± 0.09	$(1.84 \pm 0.07) \times 10^{+1}$

NOTE.—The first column is the model label, columns 2 through 5 give the mean and standard deviation for all five neutron stars, and column 6 is the integral for computing the Bayes factor.

- “I” is a “Bayes Integral” - their “goodness” statistic. LSI3 claims it is from comparison with data. It is not. This is not a valid “data analysis” method.
- Which of your “Bayesian Preferred” models are consistent with the observed X-ray spectra for the five sources, and which are not? *This is answered in every data analysis paper ever written. It is not answered in LSI3.*

Question for LSI 3

- Which of your “Bayesian Preferred” models are consistent with the observed X-ray spectra for the five sources, and which are not? In short, what are their “null hypothesis probabilities”?

This is answered in every data analysis paper ever written. It is not answered in LSI 3.

TABLE 4
PROPERTIES THE BAYESIAN MODELS

Model	M (M_{\odot})	R (km)	R_{∞} (km)	z	I
Base	1.31 ± 0.40	11.09 ± 0.39	13.8 ± 1.1	0.25 ± 0.12	$(7.32 \pm 0.37) \times 10^{-9}$
Exo	1.31 ± 0.43	9.68 ± 0.64	12.6 ± 1.8	0.31 ± 0.16	$(9.60 \pm 0.57) \times 10^{-6}$
Alt	1.17 ± 0.26	11.02 ± 0.33	13.2 ± 0.7	0.21 ± 0.07	$(5.83 \pm 0.36) \times 10^{-3}$
Exo/Alt	1.17 ± 0.26	9.81 ± 0.44	12.1 ± 0.9	0.25 ± 0.08	$(8.19 \pm 1.35) \times 10^{-1}$
H+He	1.42 ± 0.41	11.21 ± 0.76	15.0 ± 1.3	0.25 ± 0.11	$(1.46 \pm 0.08) \times 10^{-3}$
Exo/H+He	1.47 ± 0.51	11.24 ± 0.55	14.5 ± 2.1	0.29 ± 0.15	$(5.58 \pm 0.39) \times 10^{-2}$
Alt/H+He	1.34 ± 0.31	12.02 ± 0.58	14.6 ± 0.8	0.23 ± 0.09	$(1.55 \pm 0.06) \times 10^{+2}$
Alt/Exo/H+He	1.34 ± 0.33	11.48 ± 0.68	14.1 ± 1.2	0.24 ± 0.09	$(1.84 \pm 0.07) \times 10^{+1}$

NOTE.—The first column is the model label, columns 2 through 5 give the mean and standard deviation for all five neutron stars, and column 6 is the integral for computing the Bayes factor.

Partial List of Problems with LSI3

- LSI3 does not produce a statistical comparison between X-ray photon spectral data and their model. This is the only means by which any model can be tested. MAJOR
- LSI3 assumes specific absorptions (N_H values) and constrains them to be fixed. This is an inferior approach to leaving this a free parameter for the data fit (as done by G13). MINOR.
- Uncertainties in all parameters don't contain distance uncertainty, possibility of hard power-law contribution (G13 accounts for both). MINOR.

Discussions ... continued in Kyoto

International symposium on “Neutron star matter”

We will hold an **international symposium on “Neutron star matter in view of nuclear experiments and astronomical observations”** on 25th October 2013 at YITP. This symposium will be held as part of the long-term workshop on supernovae and gamma-ray bursts

<http://www2.yukawa.kyoto-u.ac.jp/ws/2013/sngrb/SN-GRB2013.html>,

where many researchers will attend. Taking this opportunity, we would like to discuss neutron star matter.



YIPQS long-term workshop

**Supernovae and
Gamma-Ray Bursts
in Kyoto, 2013**

Oct. 14-Nov. 15, 2013

YITP
YUKAWA INSTITUTE FOR
THEORETICAL PHYSICS

YIPQS
YITP K. U.

KYOTO UNIVERSITY
FOUNDED 1897

Personal Conclusion

- Steiner, Lattimer, and collaborators had been extracting constraints on the NS mass using photospheric radius expansions and qLMXBs.

$R_{\text{NS}}=10.4\text{-}12.9$ km for $1.4M_{\odot}$. Steiner et al., ApJ765,L5(2013)

$R_{\text{NS}}=11\text{-}12$ km for $1.4M_{\odot}$. Steiner et al., ApJ722, 33(2010)

- It is true that in LS13 they have adapted analytical scaling approximation for converting the G13 results to incorporate HI galactic absorption data, helium atmosphere, EOS models, etc., and claimed that the results are consistent with their previous results.
- It is one of possible interpretations of data, seeking consistency among various works, and in that view, the G13 work is not to be blamed.
- The constraints by LS13 is compatible with recent experimental and theoretical studies in nuclear physics, that, however, could not be treated to be supportive to LS13, nor to G13.
- The right answer should be obtained from various systematic works and by making more precise/newer measurements.

References

1. *MEASUREMENT OF THE RADIUS OF NEUTRON STARS WITH HIGH SIGNAL-TO-NOISE QUIESCENT LOW-MASS X-RAY BINARIES IN GLOBULAR CLUSTERS*, S. Guillot, M. Servillat, N.A. Webb, and R.E. Rutledge, [*Astrophys. J.* 772, 7 \(2013\).](#)
2. *Neutron Star Masses and Radii from Quiescent Low-Mass X-ray Binaries*, J.M. Lattimer and A.W. Steiner, [*arXiv:1305.3242 \(2013\).*](#)
3. *THE NEUTRON STAR MASS–RADIUS RELATION AND THE EQUATION OF STATE OF DENSE MATTER*, A.W. Steiner, J.M. Lattimer, and E.F. Brown, [*Astrophys. J.* 765, L5 \(2013\).](#)
4. *THE EQUATION OF STATE FROM OBSERVED MASSES AND RADII OF NEUTRON STARS*, A.W. Steiner, J.M. Lattimer, and E.W. Brown, [*Astrophys. J.* 722, 33 \(2010\).](#)
5. *Neutron star observations: Prognosis for equation of state constraints*, J.M. Lattimer and M. Prakash, [*Phys. Rep.* 442, 109 \(2007\).](#)
6. *CRUSTAL HEATING AND QUIESCENT EMISSION FROM TRANSIENTLY ACCRETING NEUTRON STARS*, E.F. Brown, L. Bildsten, and R.E. Rutledge, [*Astrophys. J.* 504, L95\(1998\).](#)
7. *Non-equilibrium processes in the crust of an accreting neutron star*, P. Hansel and J.L. Zdunik, [*Astron. Astrophys.* 227, 431 \(1990\).](#)
8. *VARIABLE THERMAL EMISSION FROM AQUILA X-1 IN QUIESCENCE*, R.E. Rutledge, L. Bildsten, E.F. Brown, G.G. Pavlov and V.E. Zavlin, [*Astrophys. J.* 577, 346 \(2002\).](#)
9. *Neutron Stars I: Equation of State and Structure*, P. Haensel, A.Y. Potekhin and D.G. Yakovlev, in *Astrophysics, and Space Science Librarly* vol. 326 (2007, Springer, New York).

Links

RIKEN mini workshop on symmetry energy, July 2013

<http://aspht1.ph.noda.tus.ac.jp/miniWS/miniWS027.html>

3rd International Symposium on Nuclear Symmetry Energy

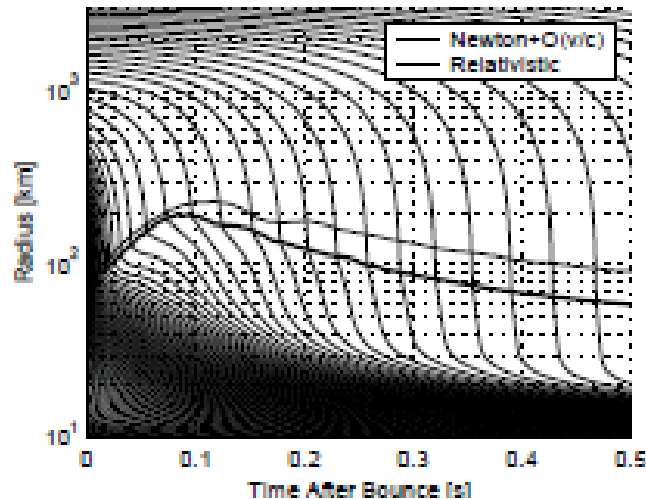
July 22 - 26, 2013

<http://www.nucl.phys.tohoku.ac.jp/nusym13/>

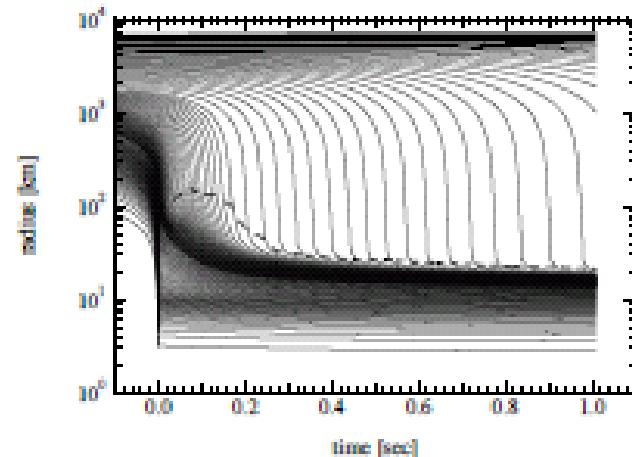
Appendix

Modern simulations with GR 1D Boltzmann ν -transfer: iron cores

canonical models: no explosion



NH $13M_{\odot}$, GR Boltzman, LS EOS+Si burning
Liebendörfer *et al.*, Phys.Rev. D63 (2001)
103004 (astro-ph/0006418 v2) Fig.6



$15M_{\odot}$, Shen EOS, Sumiyoshi *et al.*, 2005.

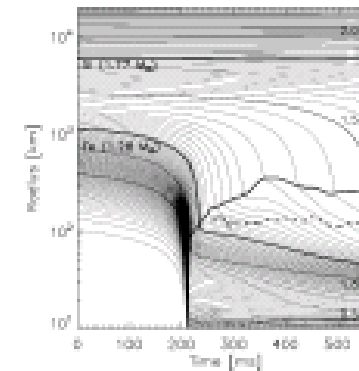


Fig. 1.— Evolution of neutron star shells as time from the start of the simulation. The shells are sequentially plotted in steps of $0.05 M_{\odot}$, and the trajectories of the outer boundaries of the iron core (at $1.28 M_{\odot}$) and of the silicon shell (at $1.77 M_{\odot}$) are indicated by thick lines. The shells is formed at 111 ms. Its position is also marked by a thick line. The dashed curve shows the position of the gain radius.

WW $15M_{\odot}$, $M_{Fe} = 1.28M_{\odot}$, NR Boltzmann
(tangent-ray method), only $\nu_e, \bar{\nu}_e$, without
 $e^-e^+ \leftrightarrow \nu\bar{\nu}$, LS EOS, Rampp *et al.*, ApJ 539
(2000) L33 Fig.1

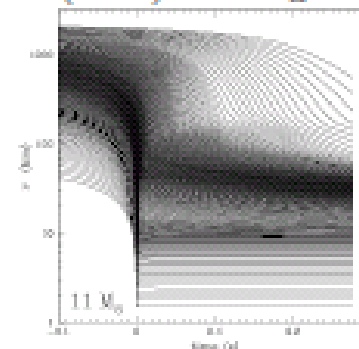


Fig. 5. Radial position (in km) of neutron star shells as a function of time (in seconds) for the 15 M_{\odot} model.

NR 1D Boltzmann ν -transfer, Thompson *et al.*,
ApJ 592 (2003) 434 Fig.5

Neutron Star Parameters

J1614-2230

P.B. Demorest et al., Nature 467, 1081(2010)

J0348+0432

J. Antoniadis et al., Science 340, 448 (2013)

Table 1 | Physical parameters for PSR J1614-2230

Parameter	Value
Ecliptic longitude (λ)	245.78827556(5) $^\circ$
Ecliptic latitude (β)	-1.256744(2) $^\circ$
Proper motion in λ	9.79(7) mas yr $^{-1}$
Proper motion in β	-30(3) mas yr $^{-1}$
Parallax	0.5(6) mas
Pulsar spin period	3.1508076534271(6) ms
Period derivative	9.6216(9) $\times 10^{-21}$ s s $^{-1}$
Reference epoch (MJD)	53,600
Dispersion measure*	34.4865 pc cm $^{-3}$
Orbital period	8.6866194196(2) d
Projected semimajor axis	11.2911975(2) light s
First Laplace parameter ($e \sin \omega$)	1.1(3) $\times 10^{-7}$
Second Laplace parameter ($e \cos \omega$)	-1.29(3) $\times 10^{-6}$
Companion mass	0.500(6) M_\odot
Sine of inclination angle	0.999894(5)
Epoch of ascending node (MJD)	52,331.1701098(3)
Span of timing data (MJD)	52,469–55,330
Number of TOAs†	2,206 (454, 1,752)
Root mean squared TOA residual	1.1 μ s
Right ascension (J2000)	16 h 14 min 36.5051(5) s
Declination (J2000)	-22 $^\circ$ 30' 31.081(7)''
Orbital eccentricity (e)	1.30(4) $\times 10^{-6}$
Inclination angle	89.17(2) $^\circ$
Pulsar mass	1.97(4) M_\odot
Dispersion-derived distance‡	1.2 kpc
Parallax distance	>0.9 kpc
Surface magnetic field	1.8 $\times 10^8$ G
Characteristic age	5.2 Gyr
Spin-down luminosity	1.2 $\times 10^{34}$ erg s $^{-1}$
Average flux density* at 1.4 GHz	1.2 mJy
Spectral index, 1.1–1.9 GHz	-1.9(1)
Rotation measure	-28.0(3) rad m $^{-2}$

Timing model parameters (top), quantities derived from timing model parameter values (middle) and radio spectral and interstellar medium properties (bottom). Values in parentheses represent the 1 σ uncertainty in the final digit, as determined by MCMC error analysis. The fit included both 'long-term' data spanning seven years and new GBT-GUPPI data spanning three months. The new data were observed using an 800-MHz-wide band centred at a radio frequency of 1.5 GHz. The raw profiles were polarization- and flux-calibrated and averaged into 100-MHz, 7.5-min intervals using the PSRCHIVE software package²⁵, from which pulse times of arrival (TOAs) were determined. MJD, modified Julian date.

* These quantities vary stochastically on $\gtrsim 1$ -d timescales. Values presented here are the averages for our GUPPI data set.

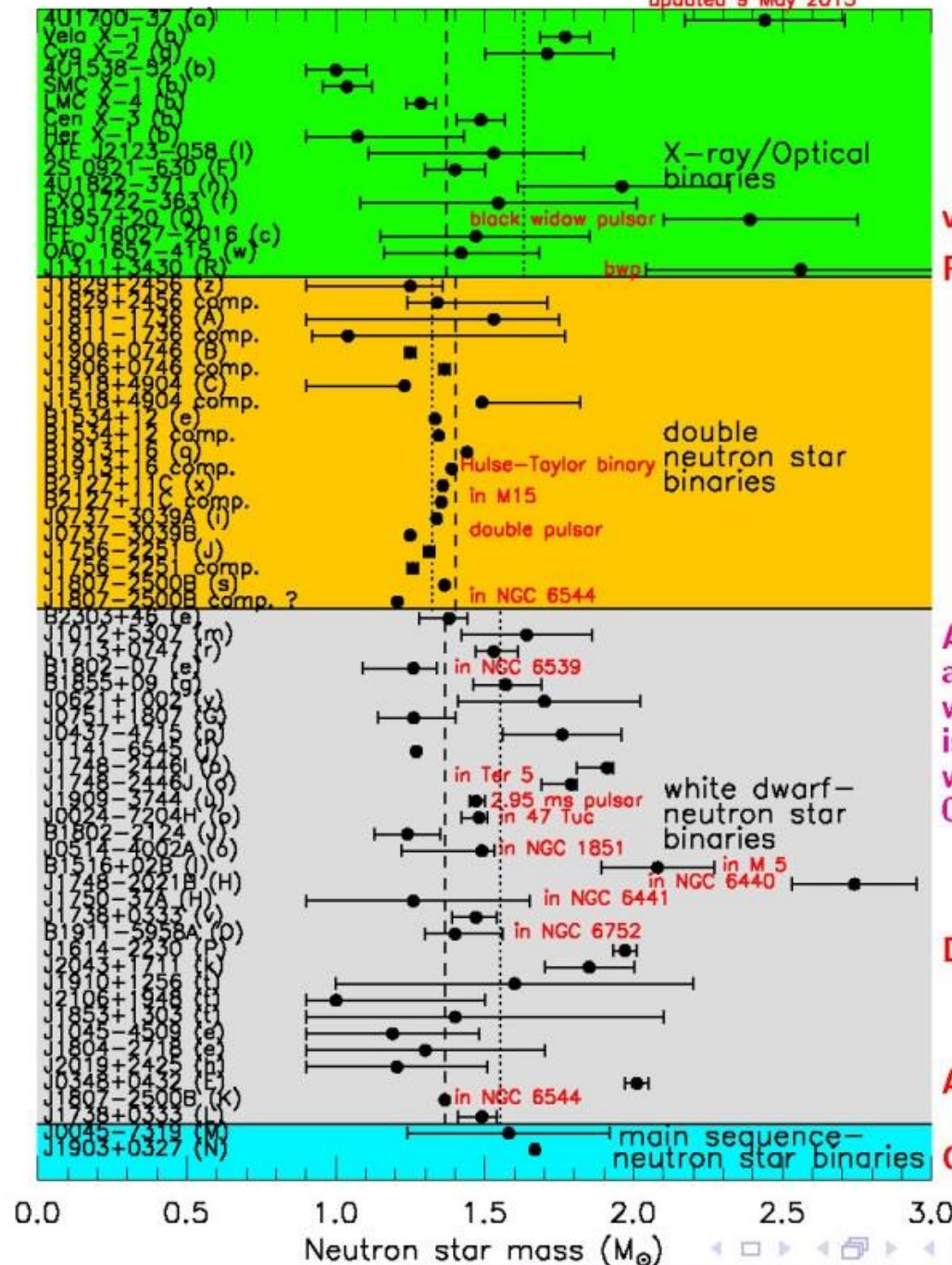
† Shown in parentheses are separate values for the long-term (first) and new (second) data sets.

‡ Calculated using the NE2001 pulsar distance model²⁶.

Table 1. Observed and derived parameters for the PSR J0348+0432 system. Timing parameters for the PSR J0348+0432 system, indicated with their 1- σ uncertainties as derived by tempo2 where appropriate (numbers in parentheses refer to errors on the last digits). The timing parameters are calculated for the reference epoch modified Julian date (MJD) 56000 and are derived from TOAs in the range MJD 54872 to 56208.

<i>Optical parameters</i>	
Effective temperature, T_{eff} (K)	10120 \pm 47 $_{\text{stat}} \pm$ 90 $_{\text{sys}}$
Surface gravity, $\log_{10}[g(\text{cm s}^{-1})]$	6.035 \pm 0.032 $_{\text{stat}} \pm$ 0.060 $_{\text{sys}}$
Semi-amplitude of orbital radial velocity, K_{WD} (km s $^{-1}$)	351 \pm 4
Systemic radial velocity relative to the Sun, γ (km s $^{-1}$)	-1 \pm 20
<i>Timing parameters</i>	
Right ascension, α (J2000)	03 ^h 48 ^m 43 ^s .639000(4)
Declination, δ (J2000)	+04 $^\circ$ 32' 11".4580(2)
Proper motion in right ascension, μ_α (mas year $^{-1}$)	+4.04(16)
Proper motion in declination, μ_δ (mas year $^{-1}$)	+3.5(6)
Parallax, π_d (mas)	0.47*
Spin frequency, ν (Hz)	25.5606361937675(4)
First derivative of ν , $\dot{\nu}$ (10^{-15} Hz s $^{-1}$)	-0.15729(3)
Dispersion measure, DM (cm $^{-3}$ pc)	40.46313(11)
First derivative of DM, $\dot{\text{DM}}$ (cm $^{-3}$ pc year $^{-1}$)	-0.00069(14)
Orbital period, P_b (day)	0.102424062722(7)
Time of ascending node, T_{asc} (MJD)	56000.084771047(11)
Projected semimajor axis of the pulsar orbit, x (lt-s)	0.14097938(7)
$\eta = e \sin \omega$	+1.9 $\times 10^{-6} \pm 1.0 \times 10^{-6}$
$\kappa = e \cos \omega$	+1.4 $\times 10^{-6} \pm 1.0 \times 10^{-6}$
First derivative of P_b , \dot{P}_b (10^{-12} s s $^{-1}$)	-0.273(45)
<i>Derived parameters</i>	
Galactic longitude, l	183. $^\circ$ 3368
Galactic latitude, b	-36. $^\circ$ 7736
Distance, d (kpc)	2.1(2)
Total proper motion, μ (mas year $^{-1}$)	5.3(4)
Spin period, P (ms)	39.1226569017806(5)
First derivative of P , \dot{P} (10^{-18} s s $^{-1}$)	0.24073(4)
Characteristic age, τ_c (Gyr)	2.6
Transverse magnetic field at the poles, B_p (10^9 G)	~ 2
Rate of rotational energy loss, \dot{E} (10^{32} erg s $^{-1}$)	~ 1.6
Mass function, $f(M_*)$	0.000286778(4)
Mass ratio, $q = M_{\text{PSR}}/M_{\text{WD}}$	11.70(13)
White dwarf mass, M_{WD} (M_*)	0.172(3)
Pulsar mass, M_{PSR} (M_*)	2.01(4)
"Range" parameter of Shapiro delay, r (μ s)	0.84718*
"Shape" parameter of Shapiro delay, $s = \sin i$	0.64546*
White dwarf radius, R_{WD} (R_*)	0.065(5)
Orbital separation, a (10^9 m)	0.832
Orbital separation, a (R_*)	1.20
Orbital inclination, i	40. $^\circ$ 2(6)
\dot{P}_b predicted by GR, \dot{P}_b^{GR} (10^{-12} s s $^{-1}$)	-0.258 $^{+0.008}_{-0.011}$
$\dot{P}_b/\dot{P}_b^{\text{GR}}$	1.05 \pm 0.18
Time until coalescence, τ_m (My)	~ 400

*For these timing parameters, we adopted the optically derived parameters (see text for details).



vanKerkwijk 2010
Romani et al. 2012

Although simple
average mass of
w.d. companions
is $0.23 M_{\odot}$ larger,
weighted average is
 $0.04 M_{\odot}$ smaller

Demorest et al. 2010

Antoniadis et al. 2013

Champion et al. 2008

0.0 0.5 1.0 1.5 2.0 2.5 3.0
Neutron star mass (M_{\odot})

Nuclear Equation of State (EOS)

EOS for Energy per nucleon

$$\frac{E}{A}(\rho, \delta) = \frac{E}{A}(\rho, 0) + S(\rho)\delta^2 + \dots$$

Symmetry energy

$$S(\rho) = J + \frac{L}{3\rho_0}(\rho - \rho_0) + \frac{K_{sym}}{18\rho_0^2}(\rho - \rho_0)^2 + \dots$$

$$\rho(r) = \rho_n(r) + \rho_p(r)$$

$$\delta(r) = \frac{\rho_n(r) - \rho_p(r)}{\rho_n(r) + \rho_p(r)}$$

Saturation Density
 $\sim 0.16 \text{ fm}^{-3}$
 $\rho_0 :$

$$L \propto P \propto R_{\text{n-star}}^4$$

(Baryonic Pressure)

Nuclear Equation of State (EOS)

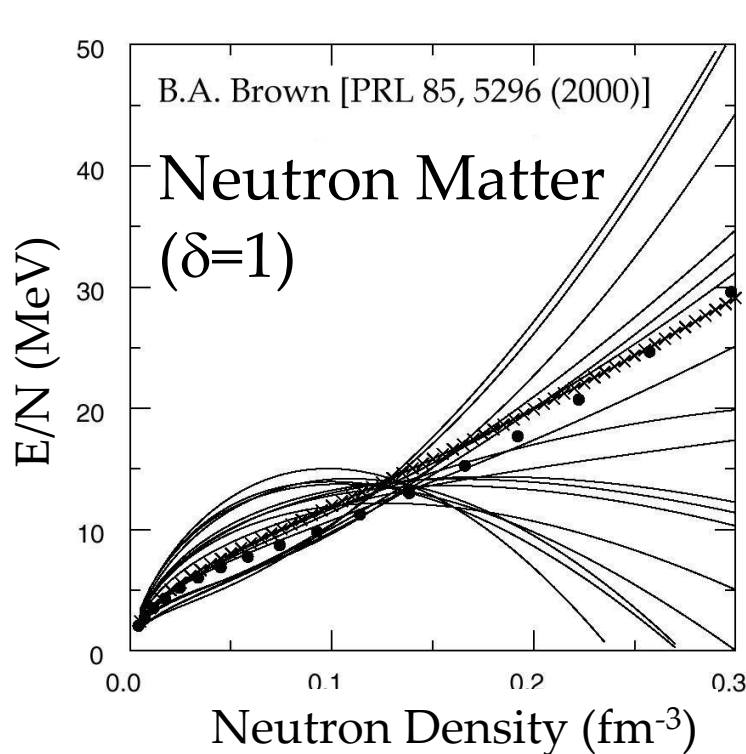
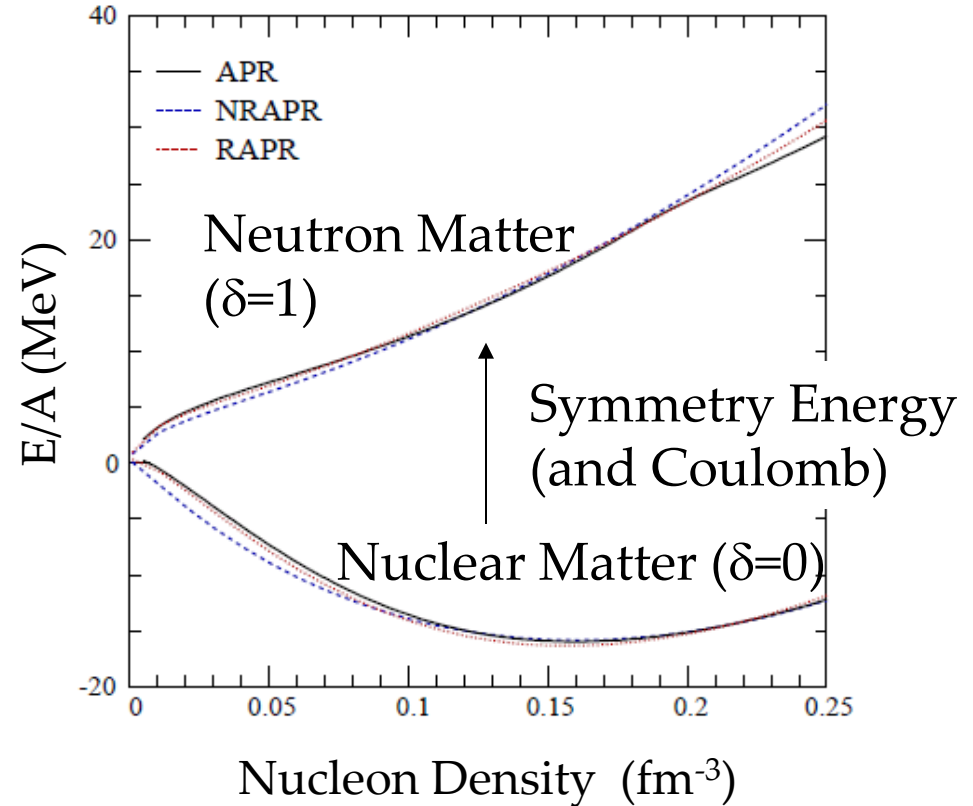


FIG. 2. The neutron EOS for 18 Skyrme parameter sets. The filled circles are the Friedman-Pandharipande (FP) variational calculations and the crosses are SkX. The neutron density is in units of $\text{neutron}/\text{fm}^3$.

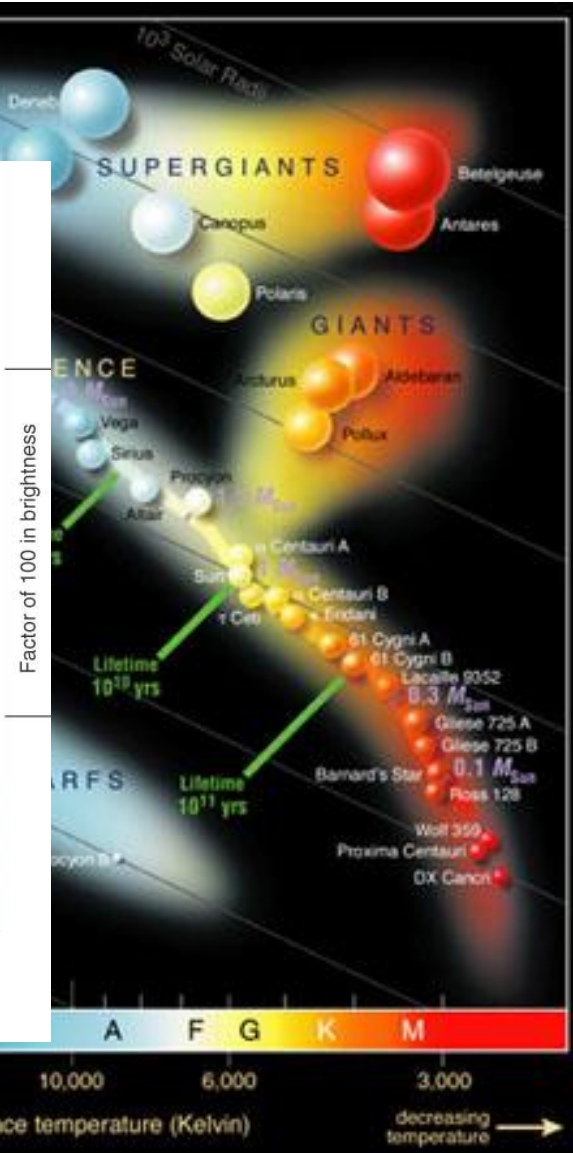
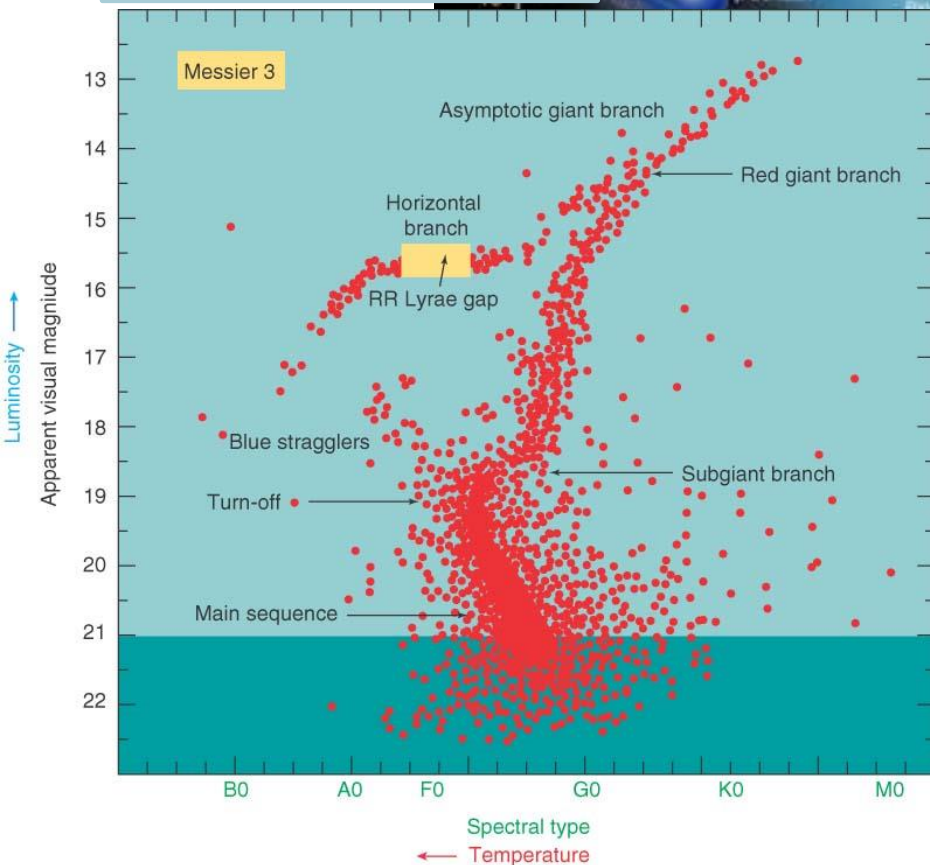


Steiner et al., Phys. Rep. 411 325(2005)

Prediction of the neutron matter EOS is much model dependent.

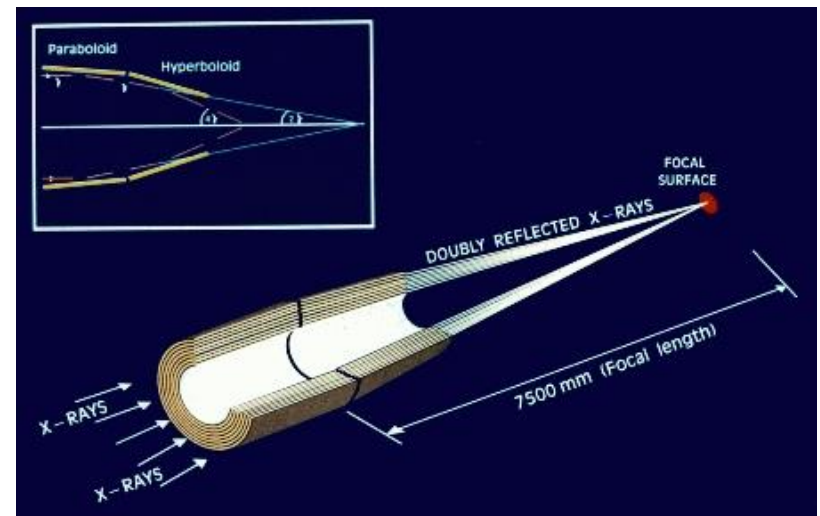
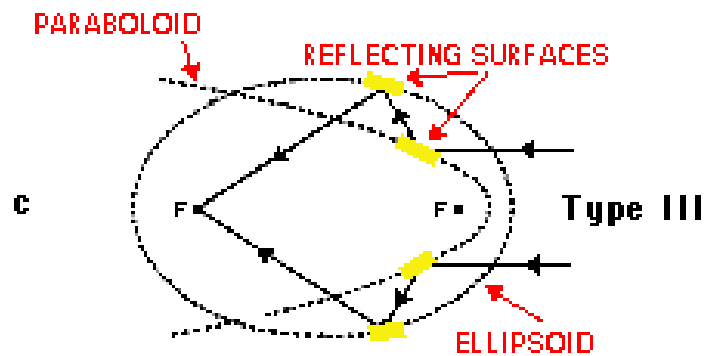
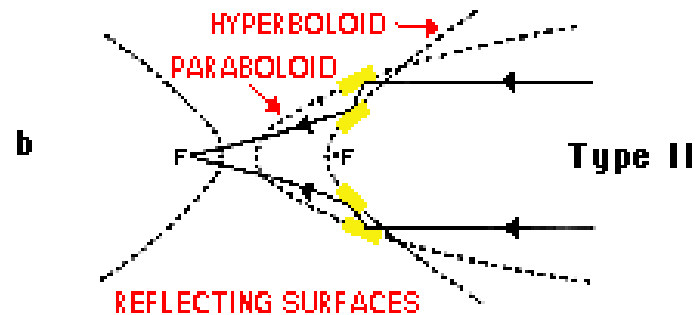
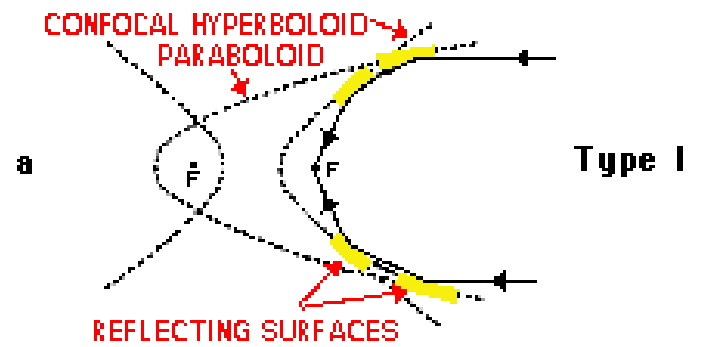
Hertzsprung-Russell (HR) Diagram

Horizontal Branch



Surface Temperature (K)

Wolter telescope





Bayes' Principle

The joint density function (同時密度関数) x and μ can be written as

$$f(x, \mu) = f(\mu | x)f(x) = f(x | \mu)f(\mu)$$

The equation can be modified as

$$\begin{aligned} f(\mu | x) &= \frac{f(x | \mu)f(\mu)}{f(x)} \\ &= \frac{f(x | \mu)f(\mu)}{\int_{\mu'} f(x | \mu')f(\mu')d\mu'} \propto f(x | \mu)f(\mu) \end{aligned}$$

Population
 μ, σ, λ

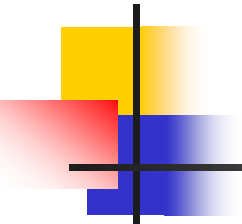
$$f(x|\mu) \quad \begin{array}{c} \downarrow \uparrow \end{array} \quad f(\mu|x)$$

Sample
 $X, E\{X\}, V\{X\}$

This equation means that the posterior probability (事後確率) $f(\mu/x)$ is calculated as a product of the prior probability (事前確率) $f(\mu)$ and the conditional probability density function $f(x/\mu)$.

The denominator is required for the normalization.

You need the prior probability distribution to calculate the posterior probability distribution.



Estimation of the true value

--- test of the H5N1 type Influenza ---

Question:

In a near future, the world is coming close to the influenza pandemic.

You got a heavy sick and went to a hospital. There, you got a test of the H5N1 type influenza, then the result was, unfortunately, positive.

You are informed of the sensitivity of the test as

If you have the H5N1 influenza ... **100.0% positive**, 0.0% negative

If you don't have the H5N1 influenza ... **99.8% negative**, **0.2% positive**

How large the probability that you have the H5N1 influenza?

Answer ?:

Even when the result is positive, you have a chance that you don't have the H5N1 influenza.

- If you have the H5N1 influenza, the probability of having the positive result is 100%.
- If you don't have the H5N1 influenza, the probability of having the positive result is 0.2%.

Then by taking the average, the probability of you to have the H5N1 influenza would be 99.8%.

$$\frac{1.000}{1.000 + 0.002} \sim 0.998$$



Assumption of a prior probability

But if you see the answer carefully, you would find that, in the discussion of the previous slide, you made an implicit assumption that the (prior) probability (before the test) of having the H5N1 influenza and the probability of not having it is 50:50.

Thus, for example, if it is known, by a national research, that the ratio of the population who have the H5N1 influenza is one out of 100,000 people (10^{-5}), the probability of you to have the H5N1 influenza is only 0.5% !

$$\frac{10^{-5} \times 1.000}{10^{-5} \times 1.000 + (1 - 10^{-5}) \times 0.002} \cong 0.005$$

→ The prior probability distribution before the test (experiment) affects the posterior probability distribution after the test (experiment).

You cannot determine the posterior probability distribution unless you assume the prior probability distribution!

**Your expectation before an experiment (or prior knowledge)
DO affect the final result!**